SANDIA REPORT
SAND99-1512
Unlimited Release
Printed March 2001

Mineralogical and Chemical Analysis of Fracture and Matrix Minerals in Selected Samples of the Culebra Dolomite

Charles R. Bryan, Malcolm D. Siegal, and James L. Krumhansl

Prepared by
Sandia National Laboratories
Albuquerque, New Mexico 87185 and Livermore, California 94550

Sandia is a multiprogram laboratory operated by Sandia Corporation, a Lockheed Martin Company, for the United States Department of Energy under Contract DE-AC04-94AL85000.

Issued by Sandia National Laboratories, operated for the United States Department of Energy by Sandia Corporation.

Available to DOE and DOE contractors from
U.S. Department of Energy
Office of Scientific and Technical Information
P.O. Box 62
Oak Ridge, TN 37831

Telephone: (865)576-8401
Facsimile: (865)576-5728
E-Mail: reports@adonis.osti.gov
Online ordering: http://www.doe.gov/bridge

Available to the public from
U.S. Department of Commerce
National Technical Information Service
5285 Port Royal Rd
Springfield, VA 22161

Telephone: (800)553-6847
Facsimile: (703)605-6900
E-Mail: orders@ntis.fedworld.gov
Online order: http://www.ntis.gov/ordering.htm

SAND99-1512
Unlimited Release
Printed November 2000

Mineralogical and Chemical Analysis of Fracture and Matrix Minerals in Selected Samples of the Culebra Dolomite

Charles R. Bryan, Malcolm D. Siegel, and James L. Krumhansl
Sandia National Laboratories
P.O. Box 5800
Albuquerque, NM 87185-0733

Abstract

Contaminant release scenarios proposed for the Waste Isolation Pilot Plant (WIPP) repository suggest that the Culebra Dolomite member of the Rustler Formation could be an important radionuclide release path. This thin, vuggy, highly fractured unit is the most transmissive geologic unit overlying the WIPP. Many of the samples obtained from drill cores in the Culebra exhibit fractures that are lined with iron-oxyhydroxide-rich and clay-rich mineral coatings. The coatings are mineralogically distinct from the rock matrix, and may have sorptive characteristics that are different from a clay-poor dolomite matrix. Where locally abundant, such coatings could affect advective/diffusive exchange between matrix blocks and fractures and the accessible mineral surface area available for radionuclide adsorption.

Clay minerals are present in the matrix and as fracture coatings in the samples from all the drill core locations examined in this study. Visual examination of rock sample surfaces in the H-19b7 core suggests that at least 7% of the total fracture surface area is coated with iron oxhydroxides or clays. In the samples from H-19b7, the amount of clay disseminated in the matrix varies from <1% to ~12 % by weight, and generally increases with stratigraphic height within the unit. In a suite of samples obtained from 12 other locations in the vicinity of the WIPP site, matrix samples from the Culebra contain 0.6–7 % clay. These samples were taken from the more transmissive lower two-thirds of the unit (Culebra Units 2-4) which was considered to be the accessible portion of the unit in the WIPP Compliance Certification Application (CCA). Clay minerals also occur as clay-rich laminae and partings with the geometries of primary sedimentary structures and dissolution residues. Such partings are the loci of bedding plane fractures, and have the heaviest clay coatings found in the unit. Crosscutting fractures also commonly exhibit clay mineral coatings, but these are generally discontinuous and much thinner.

Matrix and fracture coating clay assemblages do not show any systematic mineralogical or compositional differences. This work confirms observations made in previous mineralogical studies: corrensite is the most abundant clay mineral and comprises on average 70% of the total clay content in the samples examined. Most of the remaining clay mineral assemblage is composed of illite, with minor chlorite and serpentine; the clays occur as mixtures of very fine-grained crystallites. Although the relative proportion of illite and corrensite in these mixtures is variable over distances of a few microns, there is no consistent difference between matrix and fracture coating samples, and no variation with stratigraphic height. The amount of clay on the fracture surfaces is small, averaging 5.1 ± 4.3 grams of clay per square meter of fracture surface (lognormal mean and standard deviation) for the samples examined. The clay mineralogy and published Rb-Sr isotopic data indicate that the present clay assemblage formed during or soon after deposition of the unit by brine-induced diagenetic alteration of detrital clays. Petrographic features and similarities in the mineralogy and composition of the matrix and fracture-coating clay assemblages suggest that the clay-rich coatings on sub-horizontal fracture surfaces could be depositional while coatings on high-angle fracture are probably dissolution residues, formed *in situ* by dissolution of the dolomite matrix along the fracture walls.

Iron oxyhydroxides are also common on fractures throughout the unit. Microprobe analysis of Fe-rich fracture coatings and fracture fillings indicates that the iron phase present is stochiometrically FeOOH. Limited X-ray diffraction data show that some coatings are goethite, but variations in the color of the Fe-coatings suggest that other polymorphs of FeOOH may also be present. Pyrite (FeS_2) was commonly observed in the rock matrix.

The Compliance Certification Application (CCA) did not consider the potential effects of clay fracture skins on radionuclide transport. These effects include: 1) increased transport rates along advective flow paths due to inhibited advection/diffusion into the dolomite matrix, and 2) increased retardation due to sorption onto matrix-and fracture-coating clays. Given the thin and discontinuous nature of the fracture coatings, it is unlikely that the clay fracture coatings will have a significant hydraulic impact over distances and time scales relevant to the WIPP. However, several experimental studies have demonstrated the strong affinity of the clay minerals for uranium and other transuranic elements. This suggests that where locally abundant in the fracture and associated matrix, the clays could provide additional radionuclide sorption sites in the Culebra dolomite. Thus, the estimates of radionuclide transport rates through the Culebra given in the CCA are probably conservative.

The presence of clay-rich fracture coatings and the distribution and concentration of clay in the dolomite matrix should be considered when selecting samples for future laboratory-scale advection/diffusion experiments. Movement of a reactive tracer through hydraulically similar slices of well-indurated dolomite will vary with the clay content of the core. In laboratory-scale experiments, low permeability fracture coatings and clay-rich laminae, in addition to providing concentrations of more sorptive material, may act as low-conductivity hydraulic barriers, inhibiting advective/diffusive transport of both sorptive and non-sorptive tracers.

ACKNOWLEDGMENTS

The authors acknowledge the valuable assistance and technical knowledge of the Culebra provided by Bob Holt, who provided samples for analysis as well as many useful discussions on the origin and petrography of the unit. Reviews by Al Lappin, Sean McKenna, and Nancy Linarez-Royce significantly improved the quality of this report. John Husler and Mike Spilde of the University of New Mexico Department of Earth and Planetary Sciences provided technical support for whole-rock and electron microprobe compositional analyses.

Sandia is a multiprogram laboratory operated by Sandia Corporation, a Lockheed Martin Company, for the U.S. Department of Energy under contract DE-AC04-94AL8500.

Intentionally Left Blank

CONTENTS

FIGURES

TABLES

Intentionally Left Blank

1. Introduction

Contaminant release scenarios proposed for the Waste Isolation Pilot Plant (WIPP) repository suggest that the Culebra Dolomite member of the Rustler Formation could be an important radionuclide release path. This thin, vuggy, highly fractured unit is the most transmissive geologic unit overlying the WIPP. The hydrogeologic characteristics of the Culebra are described in the Compliance Certification Application (CCA) for the WIPP and references cited therein (U.S. DOE, 1996) and are summarized by Holt (1997). The bulk mineralogy of the Culebra at several locations has been previously described (Sewards, 1991; Sewards et al., 1991a, 1991b, 1991c; Sewards et al., 1992; Holt, 1997). Many of the vugs and fractures within samples obtained from cores from the unit are lined with iron-oxyhydroxide-rich and clay-rich mineral coatings. Sewards (1991) described the mineralogy of fracture coatings from a total of 18 samples obtained from 10 locations in the vicinity of the WIPP site. Based on a systematic examination of the entire drill core, Holt (1997) reported that coatings are abundant on ~7% of the fracture surface area in hand samples from the H19b7 test hole.

Coatings on fracture surfaces could affect both geochemical and hydrologic transport of contaminant species through fractured rock. Fracture "skins" may form by alteration of the wall rock by fracture fluids, by precipitation of minerals from fracture fluids, or by transport and deposition of fine-grained or colloidal minerals onto the surface. Because fracture skins commonly have a low hydraulic conductivity, they could change the solute transport properties of the fractured media. In double-porosity systems, they could inhibit advective and diffusive exchange between blocks and fractures, altering flow velocities within the fractures and affecting the dispersive characteristics of the modeled system (Moench, 1984, 1995; Fu et al., 1994). By inhibiting hydrologic transport into the matrix, fracture coatings could decrease the accessible mineral surface area for adsorption, thus affecting geochemical transport as well. In addition, coatings are commonly mineralogically distinct from the matrix, having adsorptive characteristics that are significantly different from that of the bulk rock.

The primary goal of this report is to examine the abundance, composition, and distribution of clay minerals from samples obtained in drill holes at several locations within the Culebra dolomite in the vicinity of the WIPP site. Although not a quantitative, systematic, site-wide study of the frequency of occurrence of clay fracture coatings, this report provides a contribution to such a determination. Samples examined in this study were chosen because of the presence of open fractures, porous vug-rich zones, or visible fracture coatings, and thus are not representative of the entire population of fractures in the Culebra. The samples came from two sources. The first set (9 samples) was collected from core of the H-19b7 drill hole in 1996 by R. Holt. These samples were chosen to document stratigraphic variations in the composition and thickness of Culebra fracture coatings at a single geographic location. Examination of this suite of samples allowed comparison of fracture coatings from the densely-lithified upper half of the unit to those from the highly fractured, vug-rich lower half. The second set of Culebra samples (21 samples) consisted of core and shaft samples from 12 other locations in and around the WIPP site, and were collected from the WIPP Core Library. The samples were chosen to document lateral variations in the fracture coatings within the Culebra in the vicinity of the WIPP site, and to qualitatively determine if the characteristics of fractures in the H-19b7 core are representative of the Culebra Dolomite at other

locations. In all, ~120 Culebra core and shaft samples from locations in and around the WIPP site were examined, and a sub-sample of 32 specimens, from ten shafts and well holes, were selected for further study (Figure 1 and Table 1). The stratigraphic positions of the samples in relation to the Culebra subunits (CU-1, CU-2, CU-3, and CU-4) defined by Holt (1997) are indicated in Table 1; the assumed boundaries of the subunits are indicated in the caption to Figure 1. In some boreholes, the boundaries of the Culebra subunits can be estimated only roughly. This uncertainty for the corresponding samples is indicated by use of italics in Table 1.

In addition to examination of fracture coatings, the compositions of clays within the matrix of the samples were examined. A comparison of the fracture coating and matrix clay compositions may prove useful in determining the origin of the fracture-coating materials. Matrix clays are probably inaccessible to the fracture-dominated flow that characterizes transport in the Culebra over short distances (Holt, 1997). However, unless the low permeability and diffusivity of clay skins significantly decrease mass transfer across fracture-matrix interface, they could be accessed by transport occurring over time scales and distances relevant to radionuclide release scenarios for the WIPP site.

The information obtained in this study can support evaluation of alternative models for radionuclide retardation and provides a basis for selection of samples for laboratory-scale sorption and advection/diffusion experiments. It will also be useful in interpreting the results of such experiments and extrapolating them to the Culebra Dolomite as a whole. The occurrence of clay minerals and iron oxyhydroxides on the surfaces of open fractures, lining vugs, and disseminated in the matrix of the dolomite should be considered in evaluating the realism of K_ds distributions assumed for the Culebra in performance assessment. Such distributions will be conservative if they are based solely upon batch experiments using cleaned, clay-poor, coating-free material (Triay et al., 1998). A comparison of the composition of clays in the Culebra dolomite with well-characterized clay from the unnamed lower member of the Rustler Formation (Sewards et al., 1992; Park et al., 1995; Prasad et al., 1998) may be useful in determining the relevance of mechanistic sorption studies using clays to the prediction of radionuclide retardation in the Culebra.

This work was carried out as using procedures listed in Analysis Plan AP-002, “Mineralogical and Chemical Analyses of Fracture, Matrix and Vug Lining Minerals in Selected Culebra Dolomite Samples Collected Prior to 1991.”

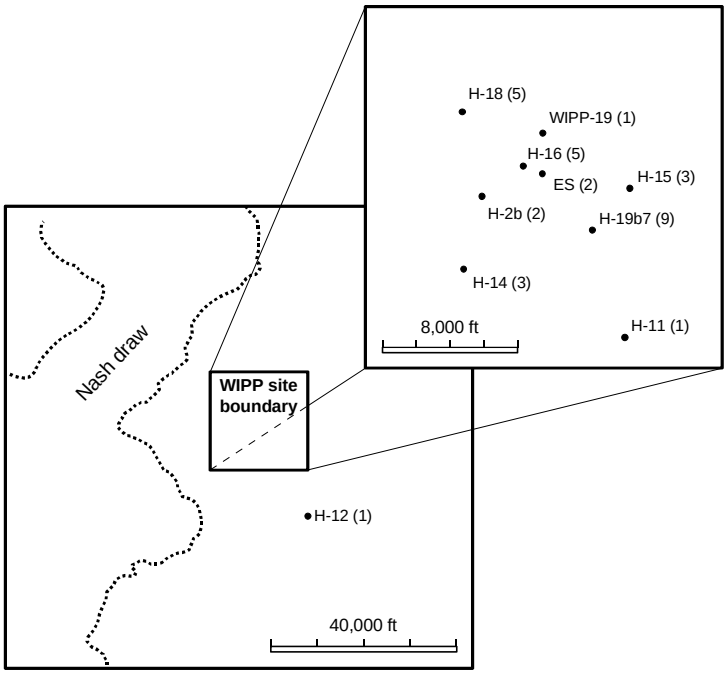

Well/core	Top of CU-1	Top of CU-2/3	Top of CU-4	Base of Culebra
H-2B	623.0	*632.8*	*642.0*	645.0
H-11	730.0	*739.9*	*749.1*	756.0
H-12	823.0	833.9	843.8	850.0
H-14	545.0	*554.8*	*564.0*	571.0
H-15	861.0	870.6	877.1	883.0
H-16	702.0	*711.8*	*721.0*	724.0
H-18	689.0	697.3	707.2	713.0
H-19	740.8	750.6	759.4	764.4
WIPP-19	756.0	766.5	775.4	779.0
Exhaust Shaft	*715.5*	*726.0*	*735.2*	*738.0*

Figure 1. Sample locations. Core samples from 10 drill holes and shafts in and around the WIPP site were analyzed. The number of samples from each location is given in parentheses. Depth (feet) of assumed tops of Culebra subunits are shown; uncertain depths are indicated in italics.

Table 1. Sample locations, depths, and general descriptions including Culebra unit.

Sample ID	Drill Hole	Depth, ft	Description (Culebra units as defined in Holt, 1997, *italics if uncertain*)
051090-22	H15	870.5	Dolomite with clay-coated sub-horizontal fracture (CU-1)
051090-26	H15	879.8	Dolomite with clay-coated sub-horizontal fracture (CU-4)
051090-28	H15	877.7	Dolomite with clay-coated sub-horizontal fractures (CU-4)
051090-44	H18	692.9	Dolomite grading into mudstone at one end, cut by heavily clay, Fe-oxyhydroxide-coated fracture (CU-1)
051090-46	H18	696.9	Vug-rich dolomite/Fe-oxyhydroxide stains on subhorizontal fracture *(CU-1)*
051090-47	H18	694.2	Vug-rich dolomite with Fe-oyxhydroxide and minor clay stains on high-angle fracture (CU-1)
051090-48	H18	695.7	Massive dolomite with clay-coated high-angle fracture (CU-1)
051090-53	H18	706.7	Fe-oxyhydroxide efflorescence on sub-horizontal fracture surface *(CU-2,3)*
051190-59	H14	547.9	Massive dolomite with selenite-filled vugs and clay-coated parting or horizontal fracture (CU-1)
051190-61	H14	553.4	Faintly bedded dolomite with clay seam, Fe-oxyhydroxide stains *(CU-1)*
051190-62	H14	554.0	Massive dolomite with Fe-oxyhydroxide and minor clay stains on high-angle fracture *(CU-1)*
051190-73	H11B3	760.1	Vug-rich dolomite; vugs lined with dark material *(CU-4)*
051190-80	H16	705.0	Massive dolomite, with clay seam and intersecting high-angle clay-coated fracture (CU-1)
051190-82	H16	708.0	Dolomite with clay stains on hummocky subhorizontal fracture (CU-1)
051190-83	H16	704.8	Massive dolomite with clay parting (CU-1)
051190-84	H16	713.2	Vug-rich dolomite with minor clay stains on hummocky subhorizontal fracture or parting *(CU-2,3)*
051190-86	H16	718.1	Vug-rich dolomite with a horizontal clay-rich parting cutting through a spongy zone *(CU-2,3)*
051190-95	Exh. shaft	720.0	Massive dolomite with heavily Fe-oxyhydroxide coated high-angle fractures *(CU-1)*
051190-98	H12	843.5	Dolomite with some vugs, high-angle fracture filled with selenite, powdery dolomite *(CU-3)*
051190-107	H2B	632.0	Somewhat vug-rich dolomite with clay-rich parting *(CU-1)*
051190-109	H2B	637.0	Vug-rich dolomite with hummocky subhorizontal fracture coated with clay, Fe-oxyhydroxides (CU-2,3)
051190-119	WIPP-19	770.1	Dolomite with clay-rich parting between dense dolomite matirix and powdery dolomite (CU-2,3)
ESM-147	Exh. shaft	721.0	Massive silty dolomite with clay-stained high-angle fracture *(CU-1)*
H19b7-742.85	H19b7	742.85	Dolomite with flat, clay-rich parting (CU-1)
H19b7-744.6	H19b7	744.6	Somewhat vug-rich dolomite with clay-rich seam (CU-1)
H19b7-752.0	H19b7	752.0	Massive dolomite with Fe-oxyhydroxide, clay-coated high-angle fractures (CU-2)
H19b7-752.2	H19b7	752.2	Vug-rich dolomite with clay-stained high-angle fractures (CU-2)
H19b7-754.7	H19b7	754.7	Spongy dolomite with hummocky, clay and Fe-oxyhydroxide stained high-angle fracture (CU-2)
H19b7-755.0	H19b7	755.0	Spongy dolomite with hummocky, clay-stained high-angle fracture (CU-2)
H19b7-757.6	H19b7	757.6	Vug-rich dolomite with clay-rich seam (CU-3)
H19b7-758.7	H19b7	758.7	Vug-rich dolomite with clay-rich seam and clay-stained high-angle fractures *(CU-4)*
H19b7-761.8	H19b7	761.8	Silty dolomite with clay-stained and partly selenite-coated high-angle fractures (CU-4)

2. Methodology

2.1 Sample Collection

Samples chosen for further analysis were comprehensively examined and described, and photographed from two or more angles to furnish an archival record of the features of interest. The approximate dimensions and weight of the sample, a visual estimate of the surface area of the surface to be sampled, and a general description of the macroscopic features of each sample were recorded. After documentation of the initial conditions, a small piece of each fracture surface was collected with a hammer and chisel. This fragment was sub-divided into two samples, one to be used for scanning electron microscope (SEM) examination of the fracture surface mineralogy and morphology, and the other for making a petrographic thin section. The fracture coatings were then collected using a high-speed rotary tool with a 3-mm diameter diamond-impregnated spherical bit (Figure 2). Grinding was done in a clear plastic bag to ensure that no fine material was lost. Two samples were collected from each surface. The first was of the fracture coating, which was collected as completely as possible, resulting in some unavoidable contamination of the sample by the underlying matrix. After collecting the fracture skin, the surface was ground clean, and the underlying matrix material was sampled over the same area. On some cores, material was collected from more than one fracture surface. The amount of material collected was small — generally 100 to 500 mg. Clay seams yielded larger samples, up to 10 grams. After collection, samples were ground with an agate mortar and pestle to an even, fine powder, and split into aliquots for X-Ray Diffraction (XRD) analysis and bulk chemical analysis.

A more complete description of sampling procedures is given in SNL WIPP TOP 554, "Visual Description, Petrographic Description, Photography, and Sub-sampling of Clay-size Materials from Culebra Dolomite Samples."

2.2 X-Ray Powder Diffraction Analysis

X-ray powder diffraction analysis was done with a Philips XRG 3100 X-ray diffractometer using Cu K_α radiation. Operating conditions are discussed in detail in SNL WIPP TOP 552, "Calibration, Use and Maintenance of Philips XRG 3100 X-ray Generator." All samples were carefully hand-ground with an agate mortar and pestle prior to analysis. Bulk fracture coating samples and bulk matrix samples were analyzed as packed-powder mounts. After bulk analysis, aliquots of 54 of the 64 total fracture coating and matrix samples (all samples for which was sufficient material) were treated with disodium ethylenediaminetetraacetic acid (EDTA) to remove carbonate and sulfate phases and water-soluble salts. The treatment was that of Moore and Reynolds (1989); an accurately weighed mass of powdered sample was boiled in 0.1 M EDTA solution for four hours at a solution:sample ratio was ≥ 50 to ensure that the capacity of the solution was not exceeded. After cooling, the solution was vacuum-filtered through a pre-weighed 0.45 µm membrane filter and repeatedly rinsed with deionized water. The filter and insoluble residue were dried and re-weighed to determine the percentage of insoluble material in the sample, and the residue was scraped off the filter with a steel spatula. If sufficient residue was recovered, sedimented mounts were made on glass slides, and another XRD pattern was generated. EDTA residues that exhibited well-defined clay peaks were treated with ethylene glycol and a third XRD pattern was generated to facilitate clay mineral identification. X-ray diffraction data were used only for qualitative

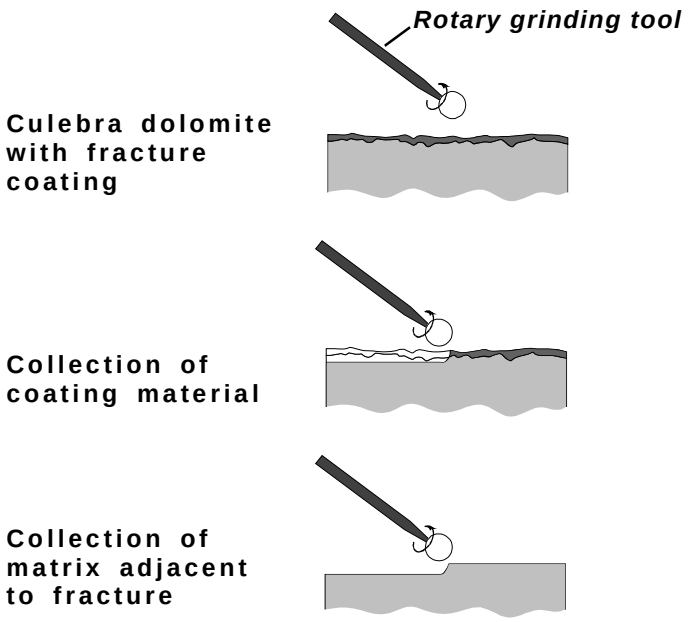

Figure 2. Technique used for collection of Culebra fracture coatings and adjacent matrix material.

identification of the minerals present. The relative abundance of each phase was calculated normatively, using the bulk chemical analyses and the normative calculations described in Sewards et al. (1991a).

2.3 Chemical analysis

Bulk fracture coating and matrix samples were analyzed for the major elements using wet chemical methods, as described in SNL WIPP TOP 553, "Procedure for Bulk Chemical Analysis of Culebra Dolomite Fracture Coatings and Matrix Material." Samples were digested with hydrofluoric and perchloric acid, then taken to dryness and redissolved in 10% HCl for analysis by atomic adsorption spectrophotometry. Separate aliquots were fused with a sodium carbonate flux and then redissolved in 10% HCl for Si and SO_3 determination. For larger samples, SiO_2 was determined using a more accurate gravimetric method. P_2O_5 and SO_3 were measured photometrically, using colorimetric and turbidometric methods, respectively. Chloride was determined by ion chromatography. H_2O^- and Loss-On-Ignition ($H_2O^+ + CO_2$) were determined by weight change after heating for one hour at 110ºC and 1000ºC, respectively. Analytical variability is discussed in Appendix A.

Three clay-rich seams yielded EDTA residues large enough for chemical analysis. However, the residues from the remaining samples were insufficient (generally a few 10's of milligrams), and were not analyzed.

2.4 Petrographic Thin Section Examination

Polished petrographic thin sections were made following the procedures outlined in SNL WIPP TOP 554, "Visual Description, Petrographic Description, Photography, and Sub-sampling of Clay-size

Materials from Culebra Dolomite Samples." They were cut perpendicular to the fracture surfaces, yielding a cross-section of the fracture and the underlying matrix. Rock billets were impregnated with epoxy following each cutting or polishing step, and kerosene was used as a lubricant to prevent dissolution of soluble minerals. Thin sections were examined under both transmitted and reflected light, and transmitted light photomicrographs were taken; several sections were later imaged with an analytical electron microprobe (AEM).

2.5 High-Resolution Imaging and Micro-analysis

Prior to analysis by scanning electron microscope (SEM) and analytical electron microprobe (AEM), samples were mounted and coated with an ~200 Å thick carbon film. The morphology of the fracture surface and of fracture coating minerals was examined with a Hitachi S-450 SEM, as described in SNL WIPP TOP 543, "Operation of the Hitachi S-450 Scanning Electron Microscope for Analysis of Fracture Coatings on Culebra Dolomite Core and Hand Samples." Imaging, Energy Dispersive Spectroscopy (EDS) elemental maps, and quantitative micro-analysis of matrix and fracture coating phases were done on polished petrographic thin sections with a JEOL 733 AEM, using Oxford Systems operating and image analysis software. Analytical variability is discussed in Appendix D.

Intentionally Left Blank

3. Results

3.1 Fractures in the Culebra Dolomite

Holt's (1997) description of the H19b7 drill core provides a detailed description of the distribution of fractures and fracture types throughout the Culebra. Holt divided the Culebra into 4 sub-units. Unit 1 comprises the upper 3 meters of the dolomite, and is characterized by well-indurated dolomite with few large vugs, although layers of microvugs are common. Fractures occur along bedding planes or as sub-vertical fractures between bedding planes. Units 2 and 3 have a combined thickness of ~3 meters, and contain abundant discontinuous interbeds of poorly-indurated "silty" dolomite. Vug-rich zones, commonly bedding-plane parallel and often highly shattered, occur locally. Nearly all vugs and silty dolomite interbeds are connected with randomly oriented fractures, forming packbreccias. Unit 4 comprises the lower ~1.5 meters of the Culebra, and consists of laminated dolomite with abundant small-scale bedding plane partings and sub-vertical fractures.

Holt (1997) found that dark or orange mineral coatings were common on both bedding-parallel and sub-vertical fractures throughout the Culebra. He observed dark mineral concentrations on about 7% of the total fracture surface area in the H19b7 core, and on about 5% of the area in units 2-4, through which most of the flow in the Culebra occurs.

Close examination of 117 hand and core samples of the Culebra dolomite, with 147 fractures exhibiting mineral coatings, has yielded the classification scheme shown in Figure 3. Fractures in the Culebra are subdivided into those where the fracture "skins" are suspected to be of primary depositional origin, such as clay-rich partings (<1 mm thick) and clay seams (up to several cm thick) along which fracturing has occurred, and high-angle and sub-horizontal fractures where the fracture skins are believed to have formed after formation of the fracture.

Within these groups, the fractures were further classified according to the composition of the fracture coatings present, as inferred from the color of the coatings. Black, gray, or dark brown partings,

Feature		A High-angle fracture	B Bedding plane fracture	C Clay-rich Parting	D Clay-rich Seam
% of total (n = 147)		52%	25%	16%	7%
Dark gray or brown material ("clay")	1	62%	67%	96%	100%
Orange/yellow material ("Fe-oxyhydroxides")	2	62%	54%	13%	0%

Figure 3. Occurrence of planar features and coatings in the Culebra dolomite. Some fracture surfaces exhibit more than 1 coating, hence, totals may be greater than 100%. See text for explanation of classification scheme.

seams and surface coatings were assumed to be clay-rich, and orange-yellow coatings, Fe-rich. Selenite and silty dolomite are very common as vug and vein fillings and fracture coatings, but were not included in the classification scheme presented here, as they were greatly under-represented in the sample set, that was chosen with a bias for clay and Fe-rich coatings. Fractures are commonly coated with more than one phase; when classifying them, the identification number of the most abundant phase is given first. For example, a sub-vertical fracture with a heavy coating of dark gray clay stains and minor orange Fe-oxyhydroxide stains would be classified as A12. Almost all fracture surfaces contain at least trace Fe mineral stains.

The classification of the samples that were analyzed for this study is given in Table 2. High-angle and sub-horizontal fractures were examined because they provide potential conduits for ground water flow. Partings and seams are zones of structural weakness in the dolomite, along which the core often separates during collection. Iron oxyhydroxide stains on parting surfaces indicate that they are commonly ground water flow-paths. The clay seams were included in this study to document any stratigraphic changes in the composition of the clays in the Culebra.

3.1.1 High-angle fractures

High-angle fractures are defined as those that cut across bedding. In the upper half of the Culebra, where the dolomite is massive and vug-poor, such fractures are often planar, while in the lower half of the unit, they commonly intersect vugs and have an irregular or hummocky topography. Crosscutting fractures commonly have very thin, discontinuous clay stains. Thicker coatings occur where the fracture intersects a clay seam and material has collapsed into the open fracture, or been sheared out along the fracture face. Clay-rich coatings on high-angle fractures are thicker and darker (black or dark brown) in the upper half of the Culebra. Those in the lower half of the unit, which contains vug-rich zones and discontinuous layers of porous, “silty” dolomite, are thinner and commonly gray in color.

Table 2. Classification of sampled surfaces.

Sample ID	Drill Hole	Depth, ft	Type	Sample ID	Drill Hole	Depth, ft	Type
051090-22	H15	870.5	**B1**	051190-95	Exh. shaft	720.0	**A2**
051090-26	H15	879.8	**B1**	051190-98	H12	843.5	**A1**
051090-28	H15	877.7	**B1**	051190-107	H2B	632.0	**C12**
051090-44	H18	692.9	**A12**	051190-109	H2B	637.0	**B21**
051090-46	H18	696.9	**A2**	051190-119	WIPP-19	770.1	**C1**
051090-47	H18	694.2	**A21**	ESM-147	Exh. shaft	721.0	**A12**
051090-48	H18	695.7	**A1**	H19b7-742.85	H19b7	742.85	**C1**
051190-59	H14	547.9	**C1 or B1?**	H19b7-744.6	H19b7	744.6	**D1**
051190-61	H14	553.4	**D1**	H19b7-752.0	H19b7	752.0	**A21**
051190-62	H14	554.0	**A12, A21**	H19b7-752.2	H19b7	752.2	**A1**
051190-73	H11B3	760.1	**Vug**	H19b7-754.7	H19b7	754.7	**A12**
051190-80	H16	705.0	**A12, D1**	H19b7-755.0	H19b7	755.0	**A1**
051190-82	H16	708.0	**B12**	H19b7-757.6	H19b7	757.6	**D1**
051190-83	H16	704.8	**C1**	H19b7-758.7	H19b7	758.7	**A1, D1**
051190-84	H16	713.2	**B1**	H19b7-761.8	H19b7	761.8	**A1**
051190-86	H16	718.1	**C1**				

Fe-oxyhydroxide and mixed clay/Fe-oxyhydroxide coatings are also common on high-angle fractures. The coatings are thin red, orange, or yellow stains; qualitatively, they are thicker and more common in the upper half of the unit. In rare cases, thick (1–2 mm) goethite efflorescences are present. These are localized at the intersection of low-angle fractures and high-angle selenite-filled veins. The nearby dolomite is corroded and pitted, suggesting that sulfuric acid was generated during formation of these efflorescences. One possible origin would be a two-step process, in which there was initially local, biologically mediated reduction of sulfate and precipitation of pyrite, followed by re-oxidation of the pyrite to produce sulfuric acid, corroding the dolomite. The iron released during breakdown of pyrite would precipitate as Fe-oxyhydroxides.

Clay-coated (A1) and Fe-oxyhydroxide-coated (A2) high-angle fractures are illustrated in Figures 4 and 5, respectively.

3.1.2 Low-angle Fractures and Partings along Clay-Rich Layers of Depositional Origin

Several criteria were used to distinguish coated low-angle or bedding plane fractures from partings along clay-rich layers of depositional origin. The fractures often cut across the bedding at a shallow angle, or are undulatory on a micro-scale, suggesting a possible stylolitic origin. In the lower half of the unit, they often cut through vug-rich layers, connecting cavities that show evidence of micro-karstic dissolution (Figure 6). Clay and Fe-oxyhydroxide coatings tend to be thin and very patchily distributed across the fracture surfaces. There is no enrichment of clay in the dolomitic material adjacent to the fracture surface. Quartz and detrital mica grains may occur in the clay coatings, but are no coarser than those in the adjacent matrix.

It should be noted that, when discussing clay-rich seams or partings of "depositional origin," the intent is not to imply that they are rich in detrital clays. As will be discussed later, the clays in the Culebra are diagenetic; the MgO-rich clay assemblage present now formed by brine interactions and alteration of the detrital clay assemblage. Thus, clay-rich depositional features were initially rich in detrital clays relative to the surrounding chemical sediments; they are now rich in clays that formed by diagenetic alteration of the detrital materials.

Clay-rich partings follow thin clay layers within the dolomite. The layers are parallel or sub-parallel to the bedding, and contain quartz and detrital mica grains coarser than those in the surrounding dolomite, indicating that they are of primary sedimentary origin. The layers tend to be somewhat undulatory on a sub-millimeter scale, and most are discontinuous, often terminating with feathered or "horsetailed" ends. Disruption and deformation of these layers may have occurred by soft sediment deformation, bioturbation, or recrystallization and dolomitization of the surrounding matrix. Clay coatings are generally evenly distributed over the parting surface, and the matrix adjacent to clay-rich partings tends to show progressive enrichment in clay towards the parting surface.

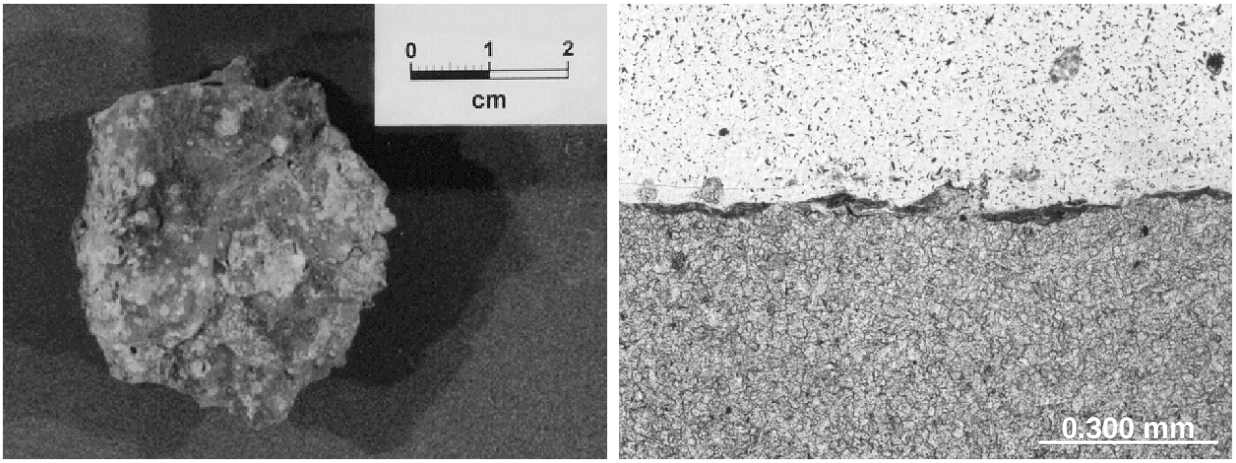

Figure 4. Clay-coated high-angle fracture, in hand specimen and photomicrograph. Sample # H19b7-752.2.

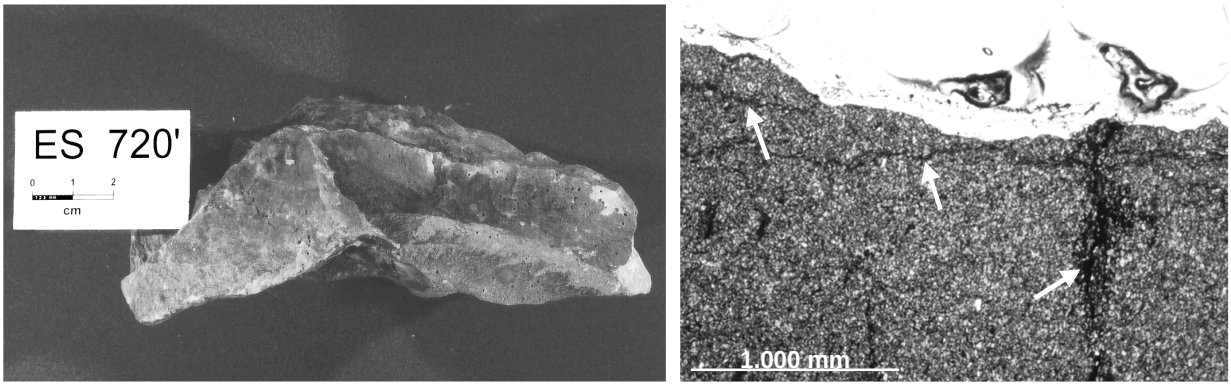

Figure 5. Fe-oxyhydroxide-coated high-angle fracture, in hand specimen and photomicrograph. Note thin Fe-oxyhydroxide-filled fractures (arrows). Sample # 051190-95.

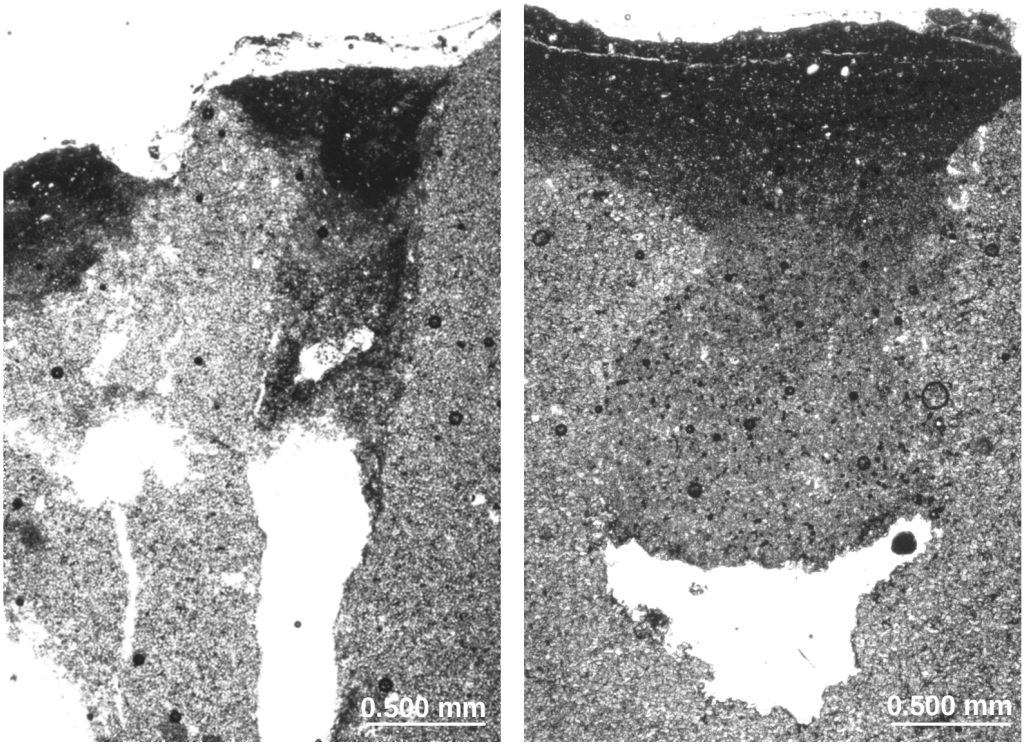

Figure 6. Micro-karstic features in the Culebra. Note that, in contrast to clay partings of detrital origin, the clay-rich dissolution residues are not enriched in quartz or detrital micas. Sample numbers: 051090-26 (left), 051190-109 (right).

3.1.3 Seams

The distinction between clay partings and seams is subjective. Clay coatings on parting surfaces tend to be very thin (generally <1 mm), while seams are commonly up to several cm thick. Clay-rich seams in the Culebra vary in character with stratigraphic height. Those in the upper part of the dolomite have planar or smoothly gradational boundaries, and are generally very dark gray or black dolomitic shales (Figure 7). Slickensided and Fe-stained surfaces within the clay and along the upper and lower contacts with the surrounding dolomite indicate that the clay seams did act as preferential flow paths.

Clay seams in the lower part of the Culebra, Holt's (1997) units 2,3, and 4, are much less enriched in clays, and are generally pale gray in color. They occur in vug-rich horizons, and are internally brecciated, with clasts of dolomite and selenite cleavage fragments in a relatively clay-rich matrix (Figure 8). They may be dissolution residues, forming in zones where high degrees of dissolution have led to fracturing and structural collapse.

3.2 Chemistry

The results of the bulk chemical analyses of surface coating and matrix samples are tabulated in Appendix A. Overall differences in chemistry between surface coatings and the adjacent matrix

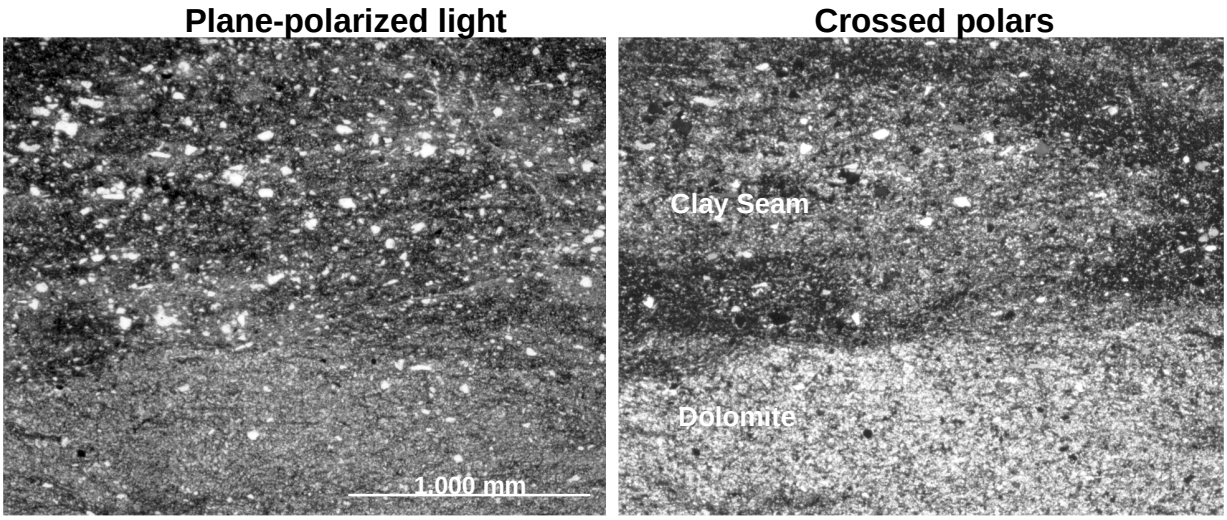

Figure 7. Boundary between a clay seam and dolomite, upper Culebra. Sample # 051190-80.

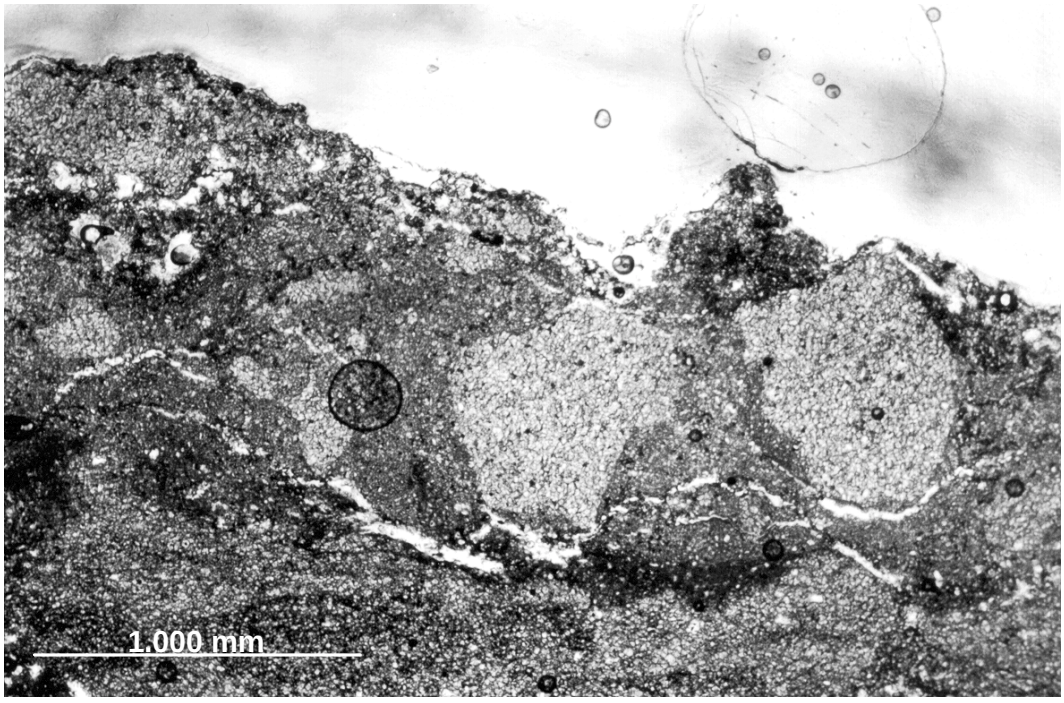

Figure 8. Dolomitic breccia with a dark, clay-rich matrix, lower Culebra. Sample # H19b7-758.7.

materials are consistent for nearly all samples, and are summarized in Figure 9. For all types of surfaces, the coatings are enriched relative to the matrix material in all elements except for Ca and Mg, the major components of dolomite. The degree of enrichment is calculated as the weight percentage of each oxide in the fracture coating sample divided by that in the underlying matrix. This suggests that quartz (SiO_2), clays (SiO_2, Al_2O_3, K_2O, etc.), and iron oxyhydroxides (Fe_2O_3*) are enriched in the surface coatings relative to the matrix material. The degree of enrichment is a function both of the composition of the fracture coating and of the amount of matrix material incorporated into the fracture coating samples during grinding, and is highly variable.

All sample coatings were enriched in Na relative to the matrix material. Chlorine contents showed sympathetic variation, indicating that halite was present on the fracture surfaces. This was confirmed when the fracture surfaces were imaged by SEM; halite was identified by energy-dispersive spectroscopy (EDS) on several of the surfaces examined. As Culebra brines are undersaturated with respect to halite, it is assumed that the halite crystallized after collection of the core, by wicking and evaporation of pore waters at the surface of the sample.

3.3 Modal Mineral Compositions

Modal mineral compositions were calculated from the chemical analyses using the method of Sewards et al. (1991a), and are summarized in Appendix C. Phases present were assumed to be clay, quartz, gypsum, dolomite, and halite. The modal clay proportion was calculated assuming an average clay composition of 15 % Al_2O_3, based upon analyses reported by Sewards et al. (1991a). A comparison of the modal clay content of the bulk sample with the amount of EDTA residue indicates that the EDTA residues are dominantly clay (Figure 10).

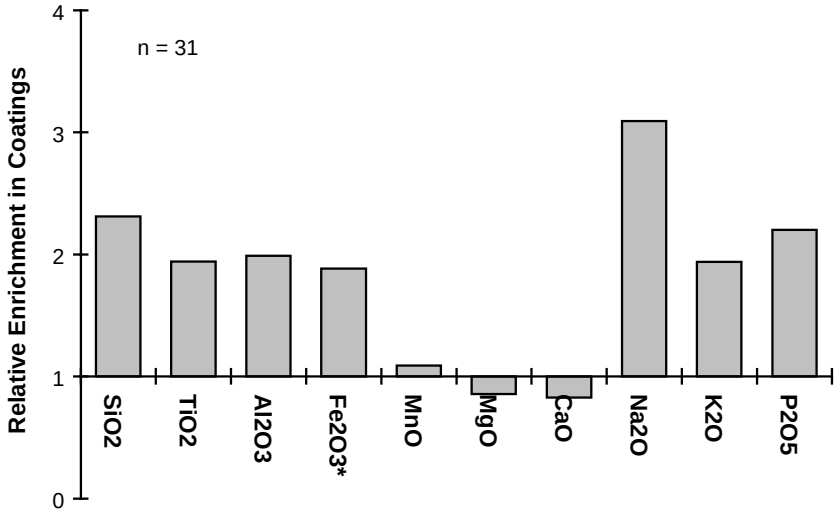

Figure 9. Average oxide enrichments in fracture coatings relative to the underlying matrix samples.

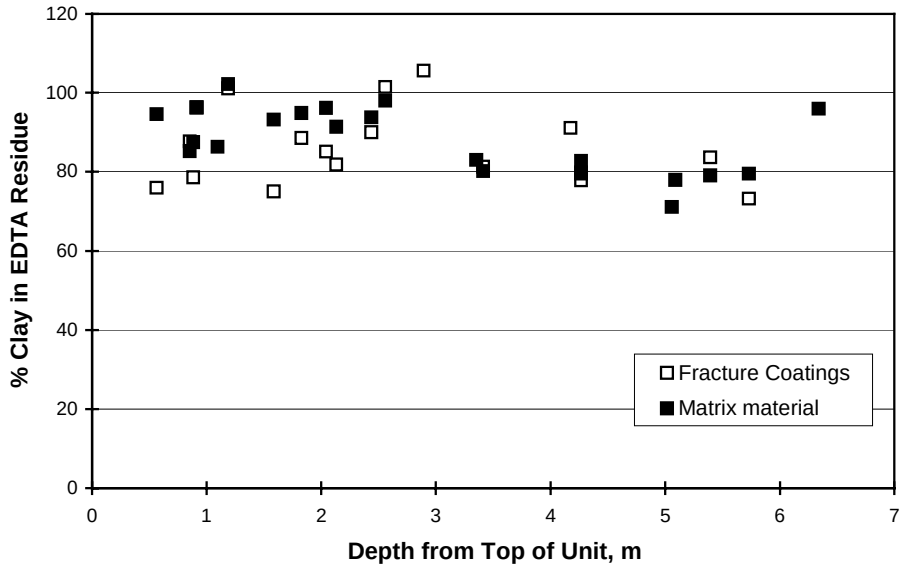

Figure 10. Variation in the estimated clay content of the EDTA residues with stratigraphic height.

3.4 Mineralogy and Petrography of Fracture Coatings and Matrix

Bulk surface coating and matrix samples were analyzed by X-ray diffraction. Aliquots of 54 samples were digested with EDTA to remove dolomite, gypsum, and halite (Moore and Reynolds, 1989) and re-examined by XRD. Several EDTA residues were glycolated and analyzed a third time to facilitate identification of the clay phases. The phases identified in each sample and EDTA residue, and the relative peak heights of each phase, are listed in Appendix B.

After each matrix and coating sample was treated with EDTA, the dissolution residues were filtered, dried, and weighed. The amount of insoluble material present in each sample is given in Table 3. Regardless of the type of surface sampled, the coatings are enriched in EDTA-insoluble minerals (quartz, clays, Fe-oxyhydroxides) relative to the matrix material.

XRD patterns of both coating and matrix samples are dominated by dolomite peaks (Figure 11). Large gypsum peaks are also common; in some samples, bassenite peaks ($CaSO_4 \cdot ½H_2O$) occur as well. Well-defined halite peaks are common in the coating samples and somewhat less common in the matrix samples. Small to large quartz peaks are ubiquitous, as are minute clay peaks at 14 Å, 10 Å, and 7 Å. The size of the clay peaks relative to those of the other phases present is a function of diffractive power rather than of abundance. For example, normative calculations (described in the previous section) indicate that the coating sample shown in Figure 11 contains about 27% clay by weight, and only about 4.5% quartz. It should be remembered that the mineralogy of the coating samples does not reflect the mineralogy of the coatings, but rather that of the coating material plus the underlying matrix, collected incidentally during sampling.

Table 3. Percentage of EDTA-insoluble residues in Culebra fracture coating and matrix samples. Values in parentheses were determined by centrifugation rather than filtering, and are less reliable.

Sample #	Hole	Depth	Type of Feature	% Insolubles		Relative Enrichment*
				Coating	Matrix	
051090-48	H18	695.7	A1	32.04	9.01	3.56
H19b7-752.2	H19b7	752.2	A1	15.10	5.82	2.59
ESM-147	ES	721.0	A12	12.59	6.61	1.90
051090-44	H18	692.9	A12	42.85	17.29	2.48
051190-62	H14	554	A12	---	12.90	---
051090-47	H18	694.2	A21	22.22	6.65	3.34
H19b7-752.0	H19b7	752.0	A21	7.89	4.66	1.69
051190-95	ES	720.0	A2	8.47	5.25	1.61
051090-46	H18	696.5	A2	---	7.18	---
H19b7-754.7	H19b7	754.7	A1(2)	4.83	6.21	0.78
H19b7-755.0	H19b7	755.0	A1	6.51	4.68	1.39
H19b7-758.7-1	H19b7	758.7	A1	7.32	4.13	1.77
H19b7-761.8	H19b7	761.8	A1	18.44	6.81	2.71
051090-22	H15	870.5	B1	24.24	7.98	3.04
051090-84	H16	713.2	B1	---	7.05	---
051090-82	H16	708.0	B12	13.93	10.75	1.30
051090-26	H15	879.8	B1	8.74	7.21	1.21
051090-28	H15	877.7	B1,C1	15.09	3.25	4.64
051190-109	H2b	637.0	B21	10.31	6.69	1.54
051190-83	H16	704.8	C1	60.06	19.08	3.15
H19b7-742.85	H19b7	742.9	C1	29.84	28.47	1.05
051190-59	H14	547.9	C1,B1	43.76	21.95	1.99
051190-86	H16	718.1	C1	---	10.44	---
051190-119	WIPP19	770.1	C1	---	3.15(2)	---
051190-107	H2b	632.0	C12	---	17.22	---
051190-61	H14	553.4	D1	32.53	13.13	2.48
051190-80	H16	705.0	D1	79.58	13.30	5.98
H19b7-744.6	H19b7	744.6	D1	(13.87)	14.36	0.97
H19b7-757.6	H19b7	757.6	D1	(5.37)	4.22	1.27
H19b7-758.7-2	H19b7	758.7	D1	5.10	4.13	1.23

* Enrichment = (% Insolubles in Coating)/(% Insolubles in Matrix)

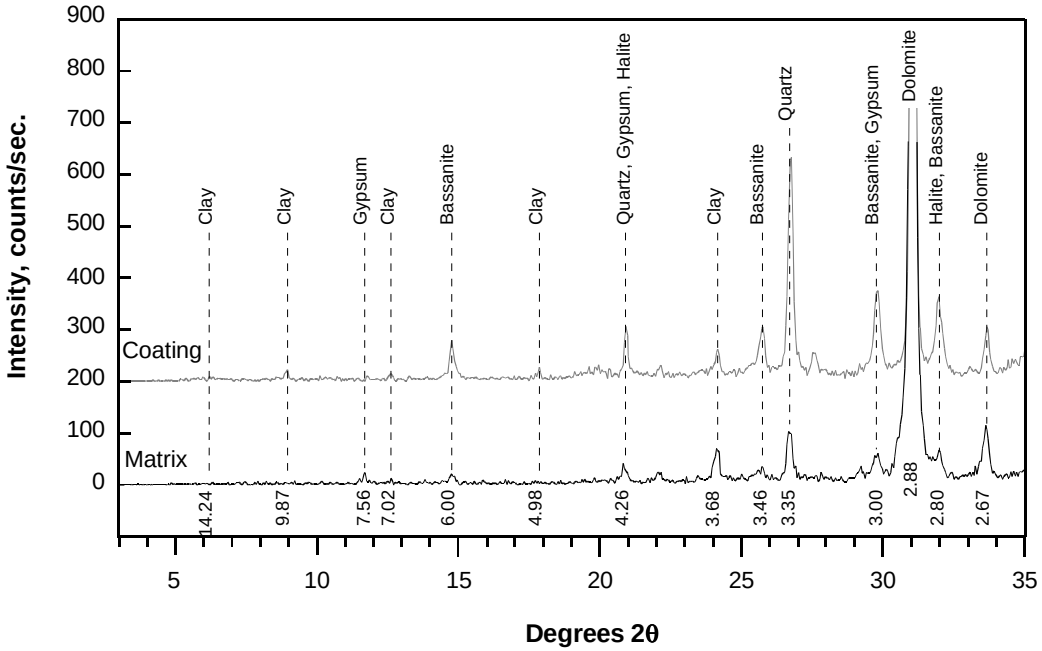

Figure 11. X-ray diffraction patterns for bulk coating and matrix samples. Sample # 051090-48.

Patterns for EDTA residues from almost all fracture coating and matrix samples are very similar, though the relative peak heights vary somewhat. Quartz peaks dominate, but this is more a function of the diffractive power of quartz than of the relative abundance of the phases present. Clay peaks are better defined in the EDTA residues than in the bulk samples. Clay minerals were identified using the techniques of Sewards et al. (1991b) and Sewards et al. (1992); identification of corrensite was verified by comparison with a standard corrensite sample (CorWa) obtained from the Clay Mineral Society Source Clay Repository (Figure 12). Corrensite is identified by an 8.8 Å peak on non-glycolated patterns; a 3.48 Å peak, often partially obscured by the main quartz peak, on glycolated patterns; the 14 Å 002 peak which shifts to 15.65 Å upon glycolation; and the 004 peak, which shifts from 7 Å to 7.8 Å. Diagnostic peaks for illite are the 001 and 002 peaks, 10.1 Å and 5.0 Å, respectively, which do not shift upon glycolation. Identification of chlorite and serpentine, and determination of their relative abundances, is difficult as many of their major peaks coincide or are obscured by those of corrensite. The 14 Å chlorite 001 peak is obscured by the broad corrensite peak, and the 7.1 Å 002 and 3.55 Å 004 peaks nearly coincide with the 001 (7.2 Å) and 002 (3.6 Å) peaks of serpentine, respectively. However, the small chlorite 003 peak at 4.75 Å is diagnostic. Serpentine was identified in those samples for which a resolvable 7.2 Å peak was present.

3.4.1 Clays

3.4.1.1 Mineralogy

Sewards et al. (1991) and Sewards et al. (1992) identified four clay minerals in the Culebra; corrensite, illite, serpentine, and chlorite. Corrensite, illite, and chlorite occur in every sample examined

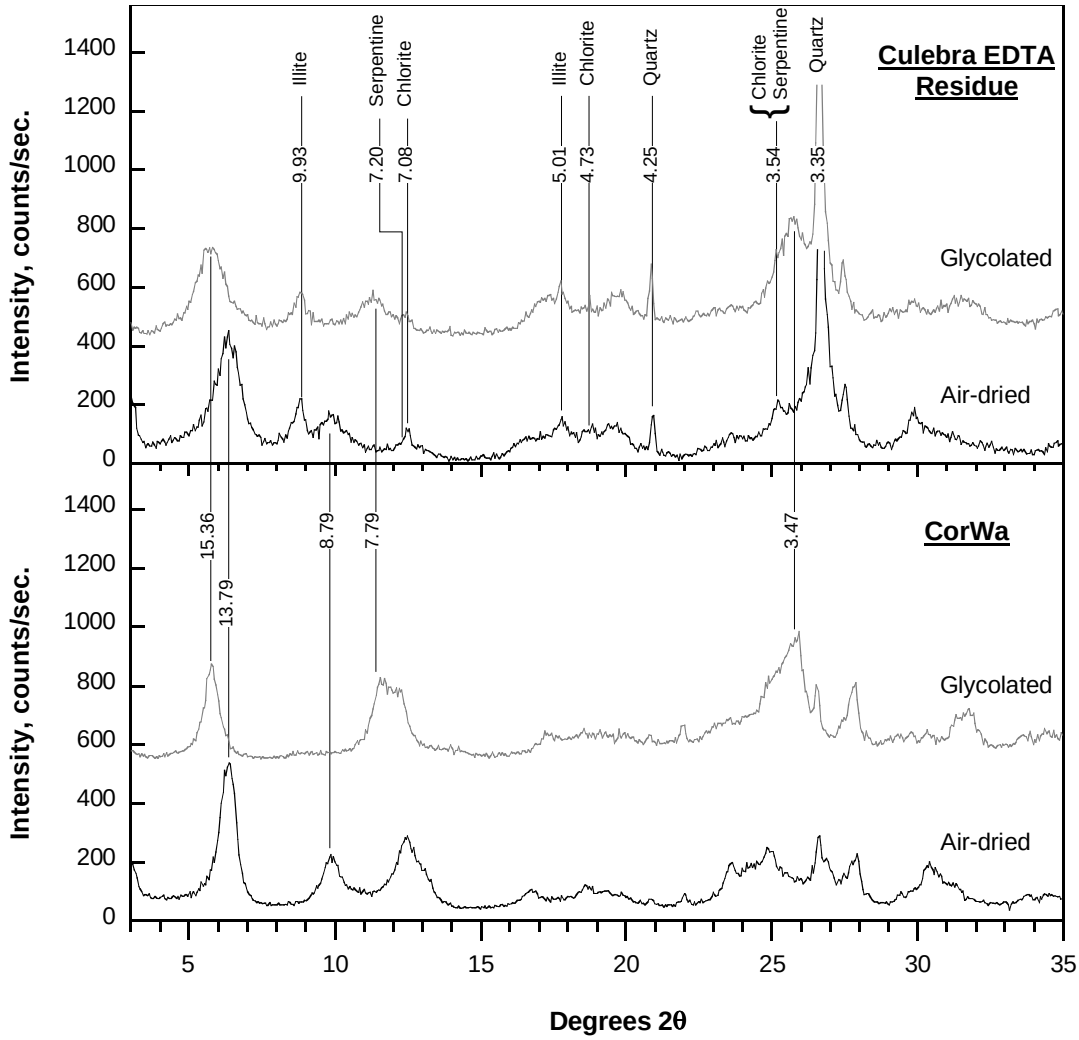

Figure 12. Air-dried and glycolated X-ray diffraction patterns for sedimented mounts of sample 051090-47-Matrix. Peaks are labeled with *d*-spacings in Angstroms. The lower plot shows the patterns for a reference corrensite; major peaks coincident to both samples are labeled.

for this study. The relative peak heights and areas on EDTA residue XRD patterns indicate that they are present in approximately the same relative proportions in all samples. Corrensite is the dominant clay mineral, with the broadest and commonly the highest X-ray peaks. The broad peaks suggest that the average crystallite size is very small. Illite is also abundant, with peaks that are occasionally as high as those of corrensite, though much narrower and smaller in total peak area. The sharp XRD peaks indicate that it is well crystallized; however, it should be noted that detrital muscovite is present in the Culebra, and is probably contributing to the illite diffraction peaks. Chlorite occurs in all samples, though peak sizes are subordinate to those of corrensite and illite. Serpentine peaks are too close to those of chlorite for clear identification, but it may be a minor phase in many samples.

3.4.1.2 Clay Analyses by Analytical Electron Microprobe

The clay phases in the Culebra are intimately intergrown, forming fine-grained mixtures of sub-micron-sized crystallites. These clay mixtures were analyzed in polished thin sections from a stratigraphically representative suite of Culebra core samples by analytical electron microprobe (AEM), using a 3 µm wide beam to minimize decrepitation and loss of alkali metals. The results are tabulated in Appendix D, and are plotted with high resolution transmission electron microscope (HRTEM) data from Sewards et al. (1992) in Figure 13. The HRTEM analyses represent the compositions of individual corrensite and illite crystallites from the Salado Formation and from the lower member of the Rustler Formation; no HRTEM data are available for clays from the Culebra. The AEM analyses of the clay mixtures from the Culebra form a mixing line between the HRTEM corrensite and illite fields, falling somewhat closer to the corrensite field. This is consistent with the XRD data, which indicates that corrensite with subordinate amounts of illite is the dominant clay assemblage in the Culebra. Although the corrensite and illite fields in Figure 13 are defined by HRTEM data from units other than the Culebra, it is unlikely that there is much compositional variation in clay compositions in the different units. Clays in both the Salado and the Rustler formed in evaporite environments, and the mixed-layer-chlorite-smectite composition is tightly constrained by the presence of corrensite x-ray diffraction peaks; such peaks only occur if the chlorite:smectite ratio is very close to 1:1 (Beaufort et al., 1997).

The illite to corrensite ratio was calculated from the AEM chemical analyses listed in Appendix D and shown in Figure 13 by assuming that the fine grained clays were two-component mixtures of illite and corrensite; chosen end-member compositions were averages of HRTEM data from Sewards et al. (1992). Illite percentages were calculated from best fits to measured MgO, K_2O, and Al_2O_3 contents. As chlorite and serpentine are compositionally much more similar to corrensite than to illite with respect to

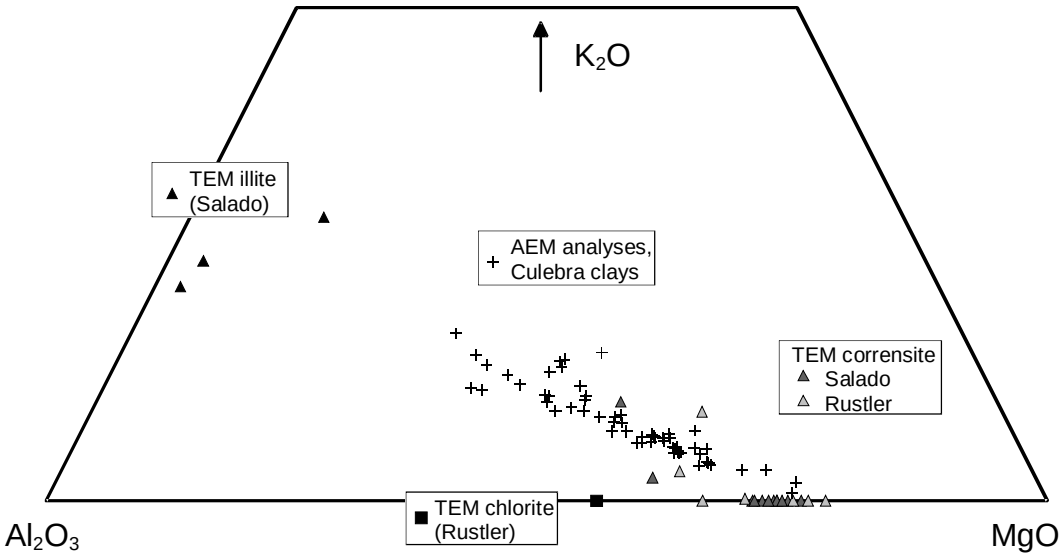

Figure 13. Clay compositions in the Rustler and Salado Formations. AEM analyses of fine-grained clay mixtures from the Culebra are shown; TEM analyses (HRTEM) of illite, chlorite and corrensite crystallites were obtained from the Salado and the lower member of the Rustler (data from Sewards et al., 1992); stochiometric serpentine plots on the MgO corner.

these three elements, the presence of these clays has relatively little effect on the calculated illite percentages. Results are shown in Figure 14. The data indicate:

1) The fine grained clays in the Culebra are 0–60% illite, averaging 29%.

2) Fine-grained clay mixtures in a single sample are compositionally heterogeneous; even analyzed points only a few tens of microns apart will vary in composition. The illite content of the fine-grained clay-mixtures varies by 20–25% in most samples.

3) There is no significant stratigraphic variation in the illite content of the fine grained clay mixtures.

4) There is no consistent compositional variation in clays in the fracture coatings relative to those in the matrix.

3.4.1.3 Distribution of Clay in the Culebra

X-ray diffraction of the EDTA residues established that clay was present throughout the Culebra. Hand sample observations suggest that clay is more abundant in the upper part of the unit, where clay-rich seams, partings, and fracture coatings are thicker, darker in color, and petrographically appear to be more pure (compare Figures 7 and 8). The chemistry of the bulk samples supports this; the modal clay content of both matrix and surface coating samples is higher in Holt's (1997) unit 1, the upper 3 meters of the Culebra (Figure 15). In this interval, measured matrix clay fractions vary from 5% to over 20%. However, the highest values were measured for matrix adjacent to partings along clay-rich layers of

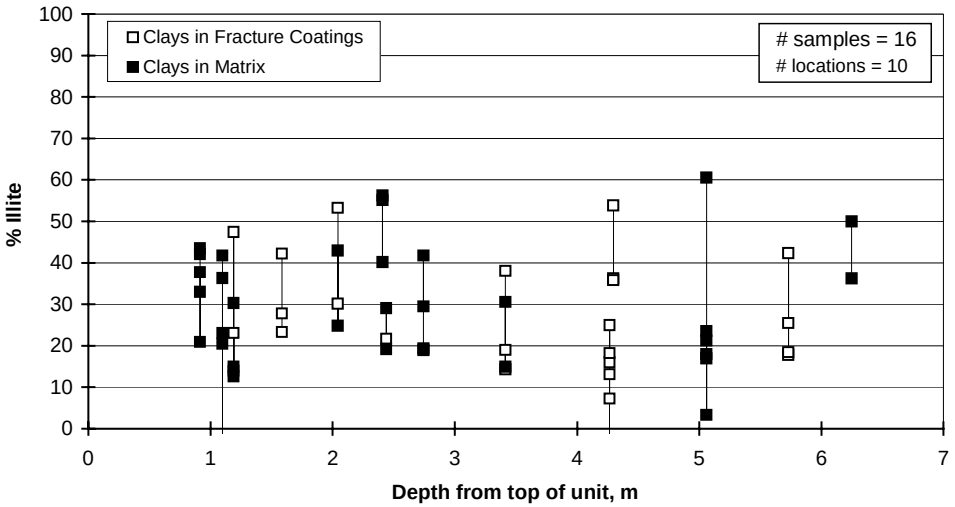

Figure 14. Modal illite content in fine-grained clay mixtures in the matrix and fracture coatings of the Culebra dolomite. Calculated from microprobe analysis of clay mixtures. Vertical lines connect data points from the same sample.

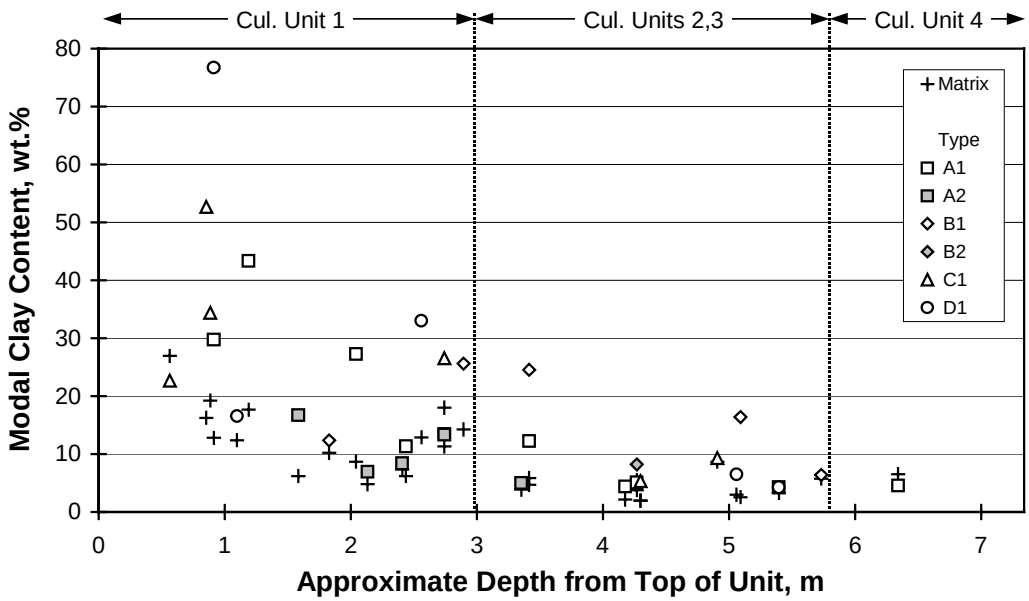

Figure 15. Modal clay content for matrix and surface coating samples plotted against depth from top of unit. Average thicknesses of Culebra subunits are indicated.

probable depositional origin, and probably indicate a gradual increase in detrital input approaching the clay-rich layer. Matrix samples adjacent to high-angle fractures are probably more typical of the bulk composition of unit 1, and vary from 5% to perhaps 12 % clay. In Holt's units 2-4, the highly fractured lower part of the unit through which most groundwater flow occurs, the matrix clay contents vary from 0.6% to 7%.

The modal clay content is calculated from the measured Al_2O_3 contents of the bulk samples, and assumes that the clay minerals contain an average of 15% Al_2O_3 (see Appendix C). An upward increase in the abundance of other Al-bearing minerals, such as muscovite and K-feldspar, could cause the observed trend. Muscovite is a common trace mineral in the Culebra, and contains ~38% Al_2O_3; if it were contributing significantly to the Al content of samples from the upper Culebra, calculated normative clay contents would be too high. However, this would result in high normative mineral totals, and in totals that vary systematically with stratigraphic height. The totals actually cluster around 100 %, and show no systematic variation with stratigraphic position. Thus, it is probable that the trend of increasing clay with stratigraphic height, shown in Figure 15, is accurate.

Clay is distributed heterogeneously throughout the Culebra on meter, centimeter, and even micron scales. Clay occurs as coatings on fracture surfaces (Figures 4 and 6), in seams and breccias up to several millimeters thick (Figures 7 and 8), and in very thin sub-horizontal partings and laminae (Figure 16). Clays are also disseminated throughout the matrix, occurring between mineral grains and in pores. Somewhat higher concentrations occur in small, fine-grained, pellet-like patches within the dolomite

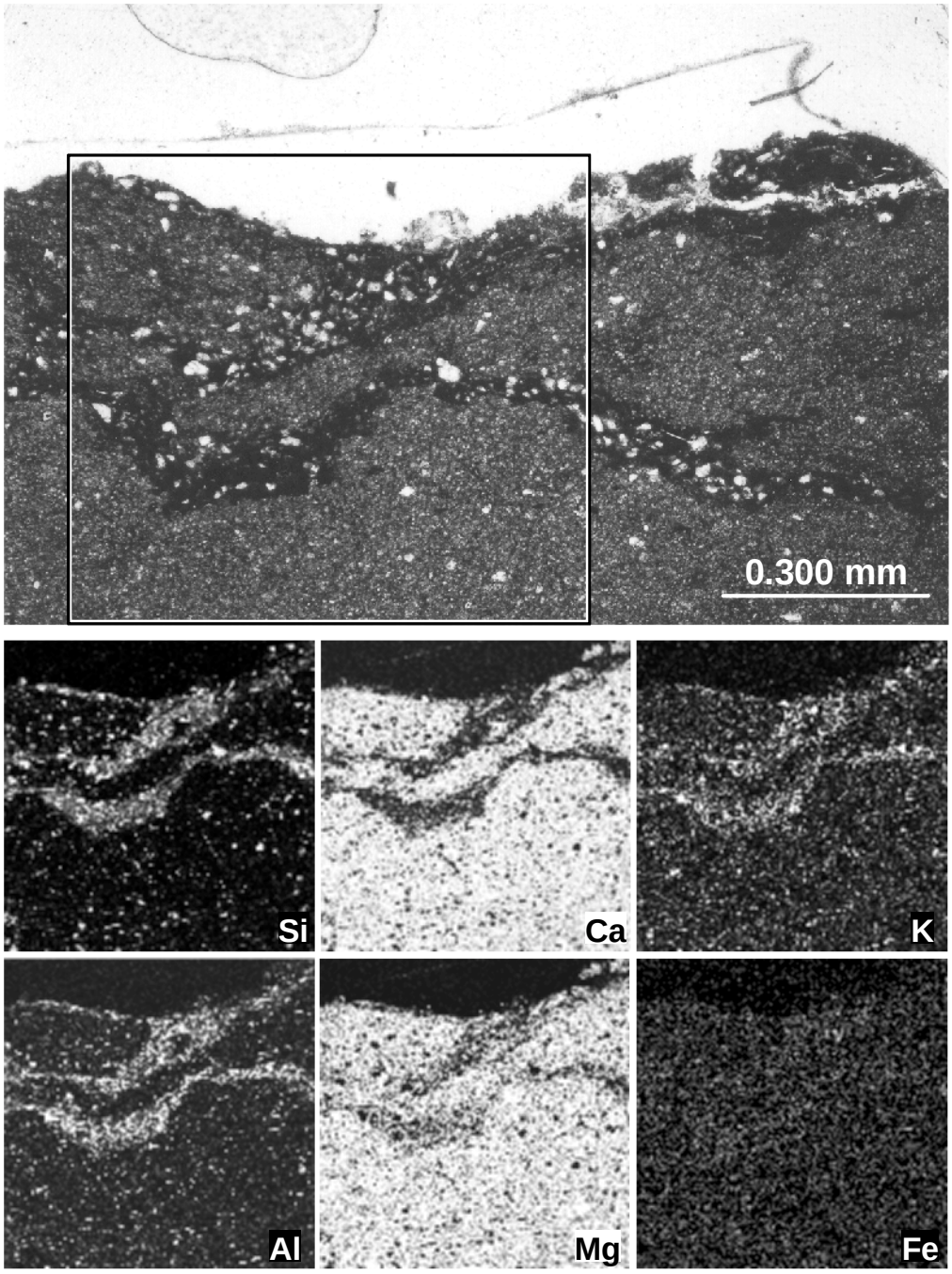

Figure 16. Photomicrograph (top) and SEM EDS elemental maps of undulate clay-rich laminae in the Culebra dolomite. Sample # H19b7-744.6.

(Figure 17), which may be fecal pellets and are abundant throughout the Culebra. Evidence that clay-coated fracture and parting surfaces were in contact with groundwater is common. Fe oxyhydroxide stains and selenite, often partly coating the clays, are abundant. In a few cases, partially cemented open fractures were observed; one such fracture, following the clay-rich boundary between well-indurated and silty dolomite, is shown in Figure 18.

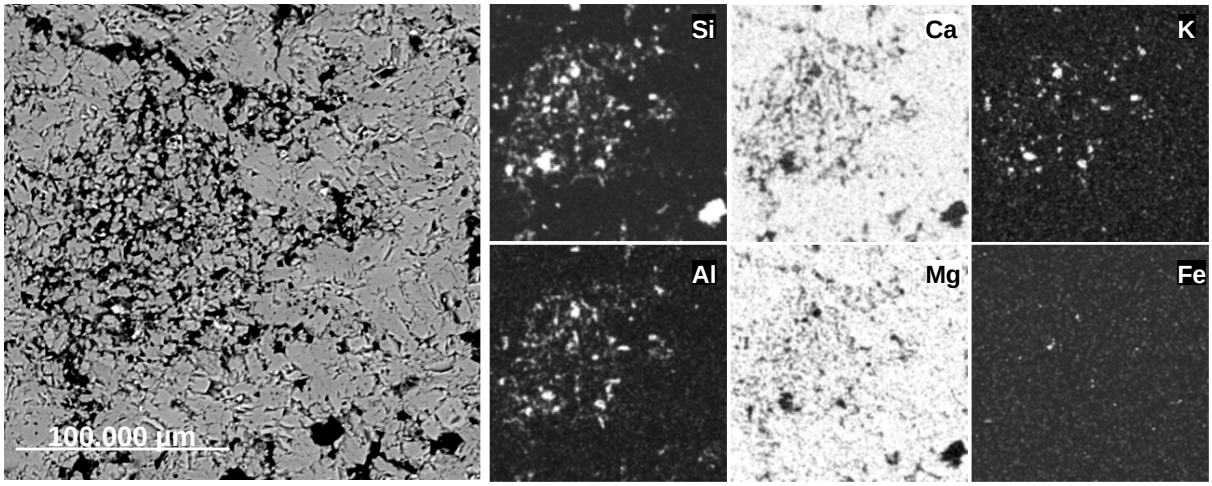

Figure 17. BSE image and EDS elemental maps of a fine-grained clay-rich patch in the dolomitic matrix of the Culebra. Sample # H19b7-752.0; see Figure 22 for photomicrograph.

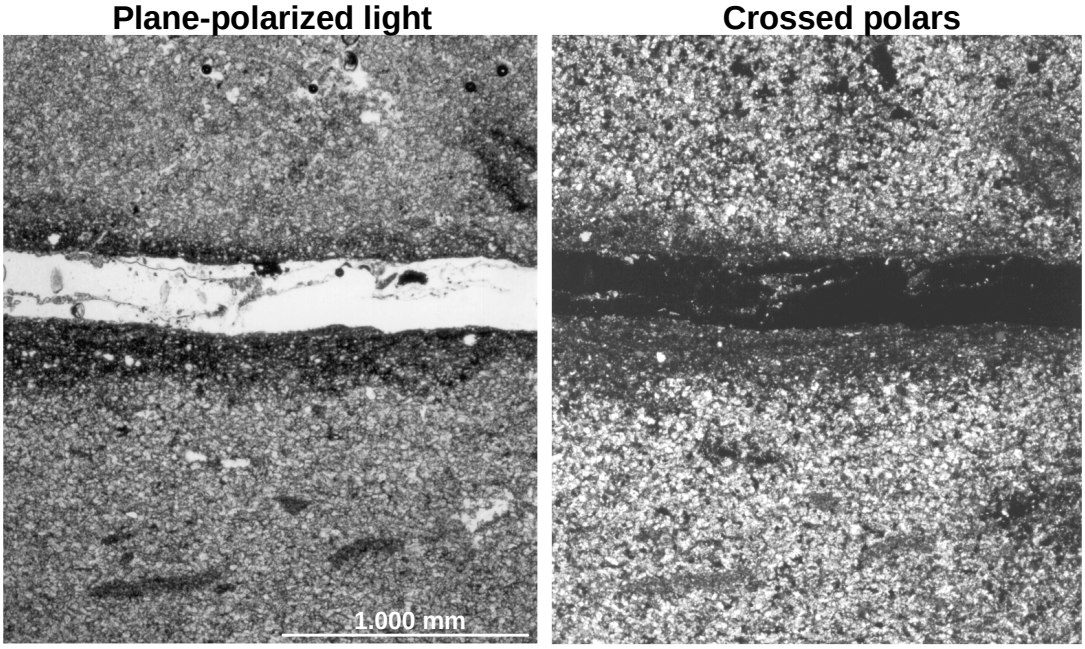

Figure 18. Open fracture following a clay-rich parting between silty, powdery dolomite (upper) and densely lithified dolomite (lower). Sample # 051190-119.

3.4.2 Fe-Oxyhydroxides

Orange, yellow, and red fracture coatings and stains are ubiquitous throughout the Culebra. SEM images indicate that the Fe-phase occurs as porous, fibrous clumps on the fracture surface (Figure 19). Only one sample, a thick orange-yellow coating, yielded sufficient EDTA residue XRD identification of the iron phase present; the material was goethite (Figure 20). Microfractures filled with Fe-oxyhydroxide were imaged and quantitatively analyzed by AEM (Figure 21); the fracture-filling material has a Fe:O ratio on 1:2, indicating that it is a polymorph of FeOOH. A somewhat thicker, multiphase Fe-oxide-rich coating is shown in Figure 22. A well-crystallized polymorph of FeOOH is present, surrounded by a rim of poorly crystalline Fe oxyhydroxide, possibly ferrihydrite, which lost water during electron beam analysis and provided a low total. The framboidal morphology of the core material suggests that it may have replaced pyrite. The Energy Dispersive System (EDS) elemental maps show that dolomite, potassium feldspar, and quartz are also present in the fracture coating. A thin clay selvage occurs between the Fe-rich fracture coating and the matrix dolomite, along which the Fe-rich coating separated from the matrix during thin section preparation.

While Fe-oxyhydroxides have precipitated on fracture surfaces, and fine-grained clay mixtures on those surfaces commonly have elevated iron concentrations due to admixed Fe-oxyhydroxides (Appendix D), Fe-oxyhydroxides are not found in the well-indurated dolomitic matrix. The clay mixtures in the matrix of the dolomite never have admixed Fe-oxyhydroxides. This suggests that fluids in the matrix are reducing relative to those in the fractures. The oxidation conditions in the matrix are probably buffered by the ~0.2% ferrous iron in the dolomite, and diffusion of oxygen into and out of the matrix is too slow to result in equilibration between the fracture and matrix fluids.

This point is further illustrated by the microfracture shown in Figure 23. This small open fracture follows a thin clay stringer in the dolomite; the parting is horizontal in orientation, and may be a primary depositional feature. The Fe element map shows that Fe is enriched not along the margins of the microfracture but rather at the boundary between the clay and the dolomite. The iron content of the fine-grained material is high (~35 %, see Appendix D), and the iron is probably present as fine-grained oxyhydroxides, as the clay compositions plot with others from the Culebra in Figure 13. The distribution of Fe is probably a result of interaction between matrix and fracture fluids, diffusion of oxygen into the surrounding material from the fracture, and diffusion of ferrous iron out of the dolomitic matrix and into the clay bordering the fracture. That the Fe is concentrated at the boundary between the clay and the dolomite, rather than along the fracture, suggests that diffusion of oxygen out of the fracture and into the clay layer is more rapid than diffusion of Fe^{+2} out of the well-indurated dolomite and into the clay.

3.4.3 Dolomite

Dolomite is the most abundant phase in most of the samples analyzed. This does not indicate that the fracture coatings are dominantly dolomite; rather it is a function of the amount of matrix material incorporated into the coating samples during sample collection with the rotary grinding tool (see Figure 2). Dolomite is the most abundant matrix mineral, and also commonly occurs in clay-rich seams, and partings. It is somewhat less common in high-angle fracture coatings.

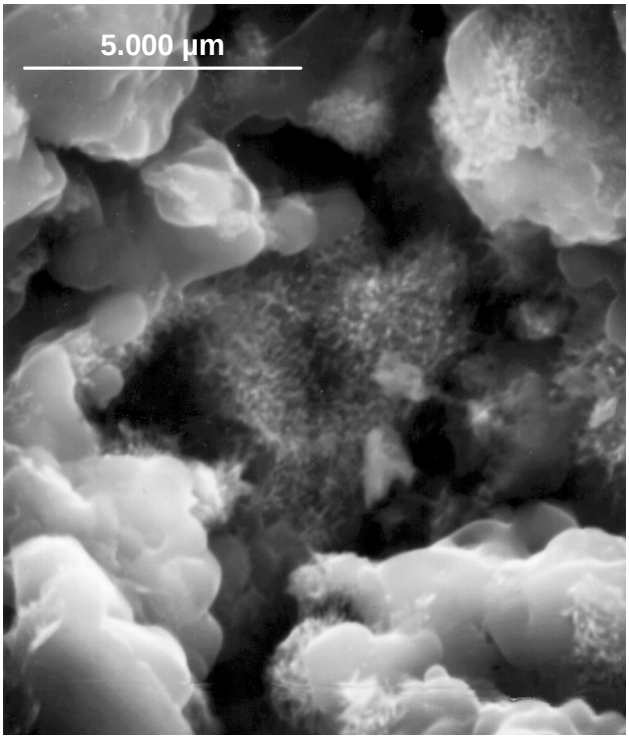

Figure 19. SEM photograph of a fibrous Fe-oxide/hydroxide phase on a high-angle, Fe-oxyhydroxide enriched fracture surface (Sample # 051190-95).

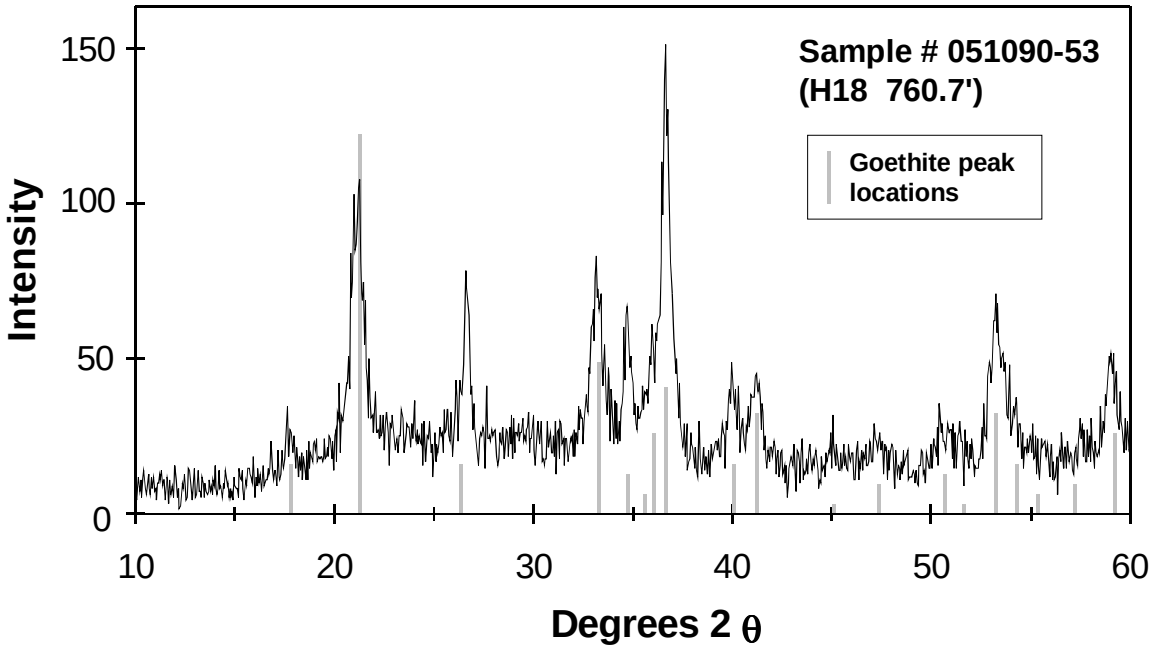

Figure 20. X-ray diffraction pattern of the EDTA residue of an Fe-oxyhydroxide-rich fracture coating sample, 051090-53.

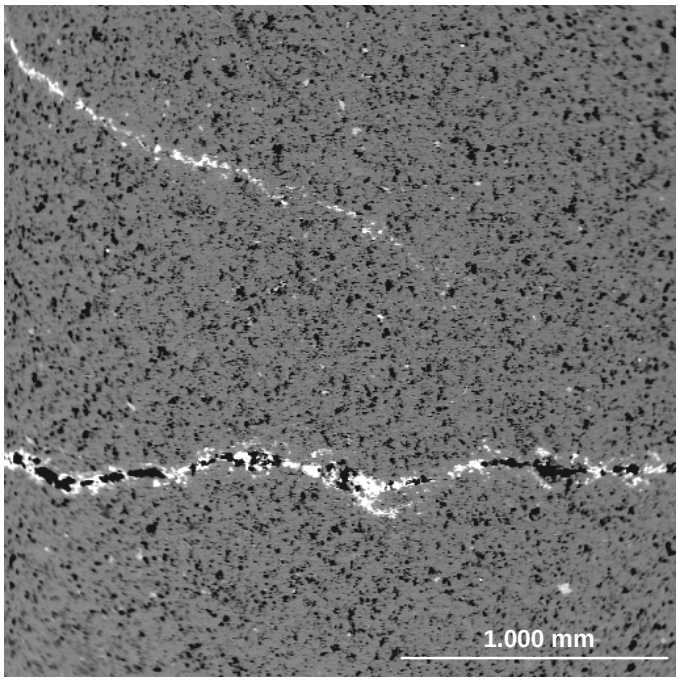

Figure 21. SEM image of Fe-oxyhydroxide-filled fractures (bright areas) in well-indurated dolomite. Note open porosity along the fractures. Sample # 051190-95.

Sewards et al. (1991b) presented microprobe analyses of dolomite compositions from 6 samples of the Culebra dolomite, from two different cores. They found that Ca/Mg ratios in the dolomite fell between 1.0 and 1.1, but cautioned that since only six samples from two cores were examined, it was not safe to make assumptions about the composition of the Culebra in general. The Ca/Mg ratio yields information on the genesis of the dolomite, and is important in developing a model for phase equilibria in Culebra brines. The average Ca/Mg ratio in dolomite from the Culebra can be derived from the bulk chemical analyses presented here. Major Ca-bearing phases in the Culebra are dolomite, clays, and gypsum (anhydrite). The measured SO_3 content can be used to correct for Ca bound up in gypsum, leaving only that in clays and dolomite. A gypsum-free Ca/Mg ratio can then be calculated, which, when plotted against Al_2O_3 (present only in the clays), yields a linear trend, the zero intercept of which is the Ca/Mg ratio of the dolomite (Figure 24). Though there is some scatter, the Ca/Mg ratio of dolomite in the Culebra is 1.0–1.1, consistent with those ratios measured directly by Sewards et al. (1991b). Note that calcite cannot have contributed significantly to any of the samples, as this would have yielded much higher Ca/Mg ratios. A similar treatment can be used to determine the amount of Fe in the dolomite, which has important implications for the oxidation state of fluids traveling through the Culebra. Sewards et al. (1991b) reported about 0.2 weight percent ferrous iron in the dolomite; once again, this was based on only six analyses. In most samples, the major iron-containing phases in the Culebra are dolomite and clays. The measured bulk Fe_2O_3* (total iron as Fe_2O_3) concentrations are plotted against Al_2O_3 in Figure 25. The data form a linear mixing trend between dolomitic, clay-poor samples and EDTA dissolution residues from clay seams (Figure 25). Extrapolation to clay-free dolomite (0% Al_2O_3) indicates that it contains about 0.22 % Fe_2O_3* (equivalent to 0.20% FeO).

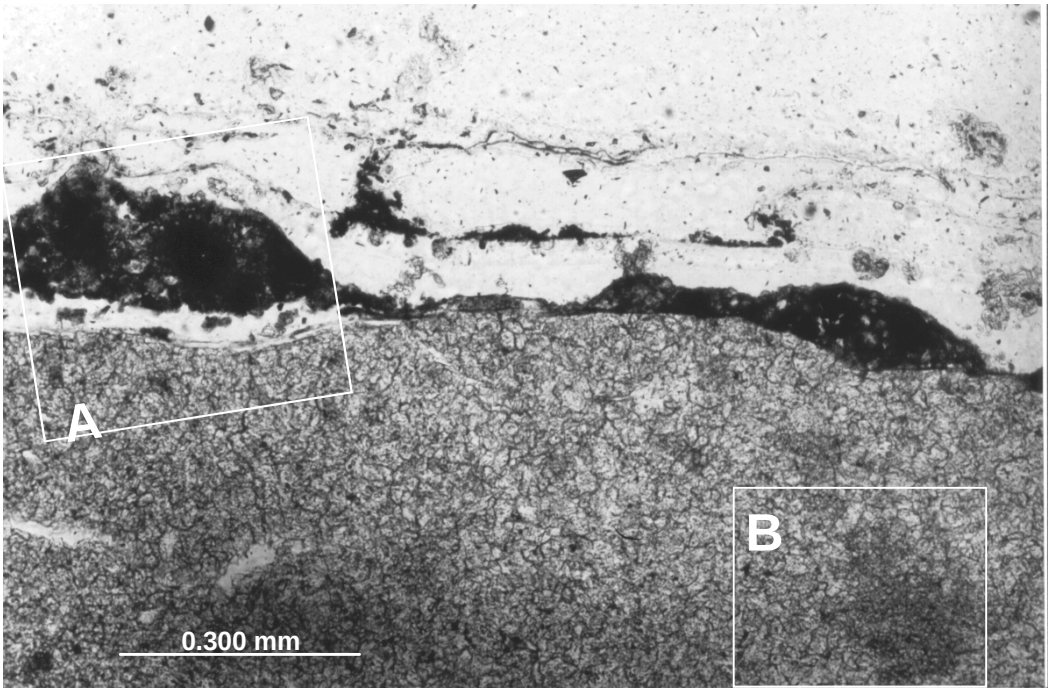

Figure 22a. Photomicrograph of sample # H19b7-752.0, showing an iron-rich coating on a high-angle fracture, and a fine-grained, patch in dolomitic matrix (Area B). EDS elemental maps of Area A are shown in Figure 22b; Area B was discussed earlier (see Figure 17).

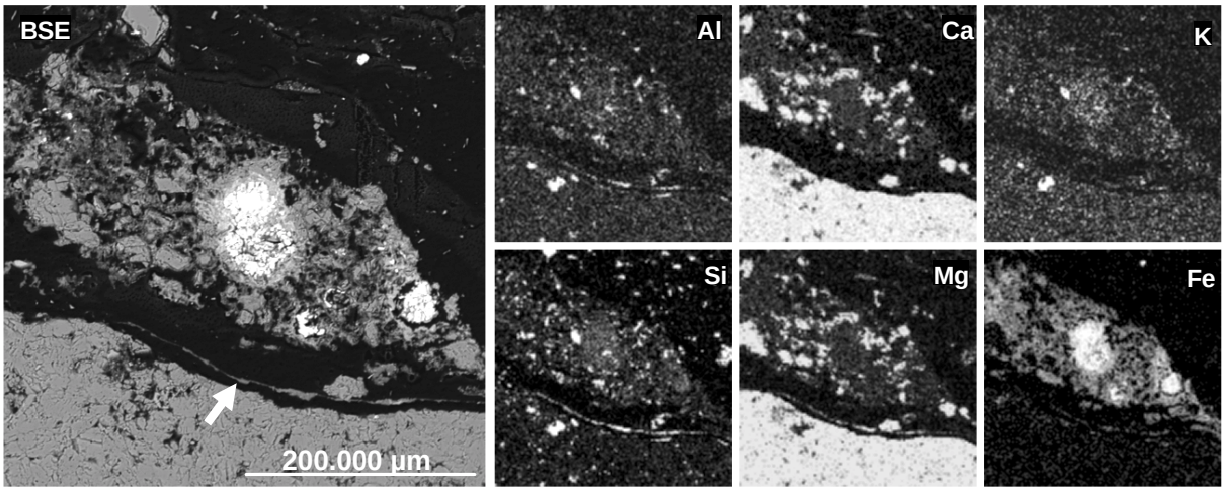

Figure 22b. Backscattered electron (BSE) image and EDS element maps for area A, Figure 22a. Note the thin clay selvage (arrow), along which the fracture coating separated from the dolomite during thin section preparation. In a BSE image, lighter areas indicate a higher average atomic number; in an element map, they indicate higher concentrations of the element of interest.

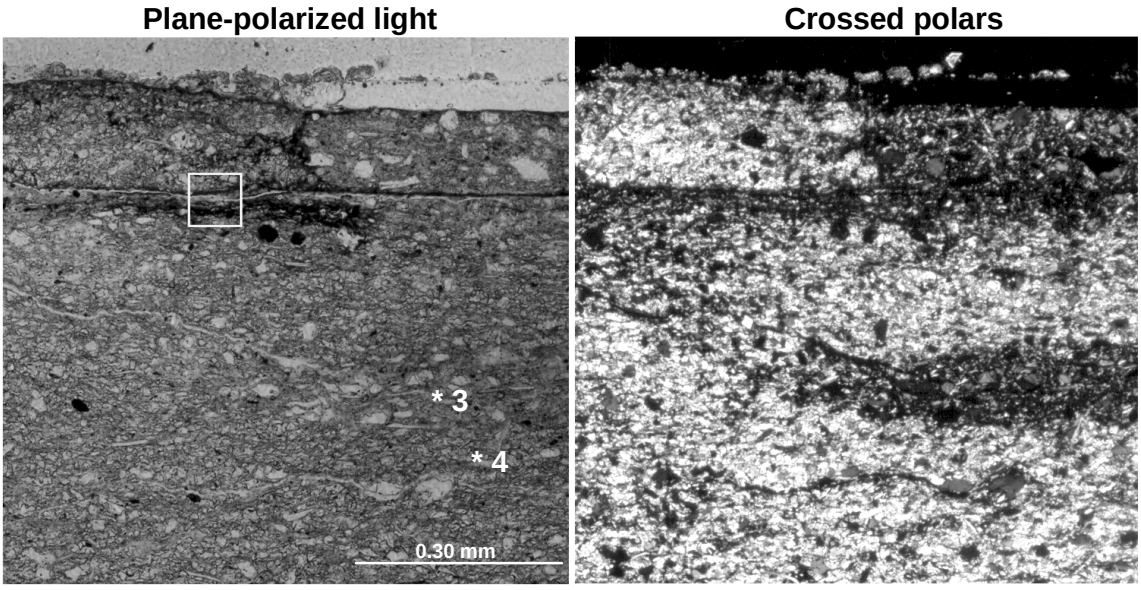

Figure 23a. Fe-stained clay-rich partings in Culebra dolomite. The upper surface is a clay-rich parting. A second parting, with an Fe-stained microfracture, parallels the surface. Numbered points are locations of clay-microanalyses (Appendix D). Sample # 051090-48.

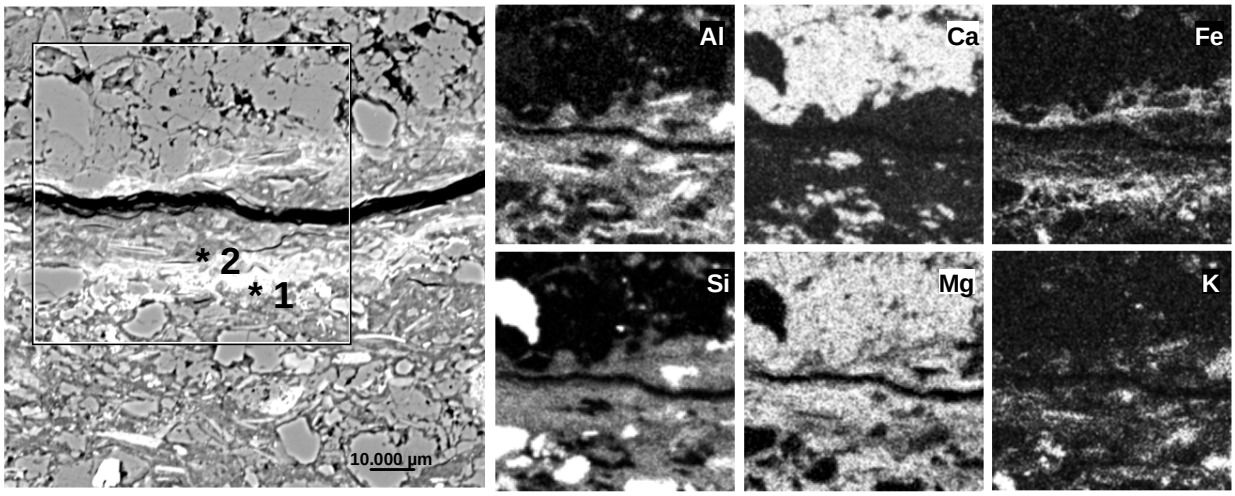

Figure 23b. Back-scattered electron image and EDS elemental maps of area marked by square in Figure 23a. Numbered points are locations of clay microanalyses (Appendix D). Sample # 051090-48.

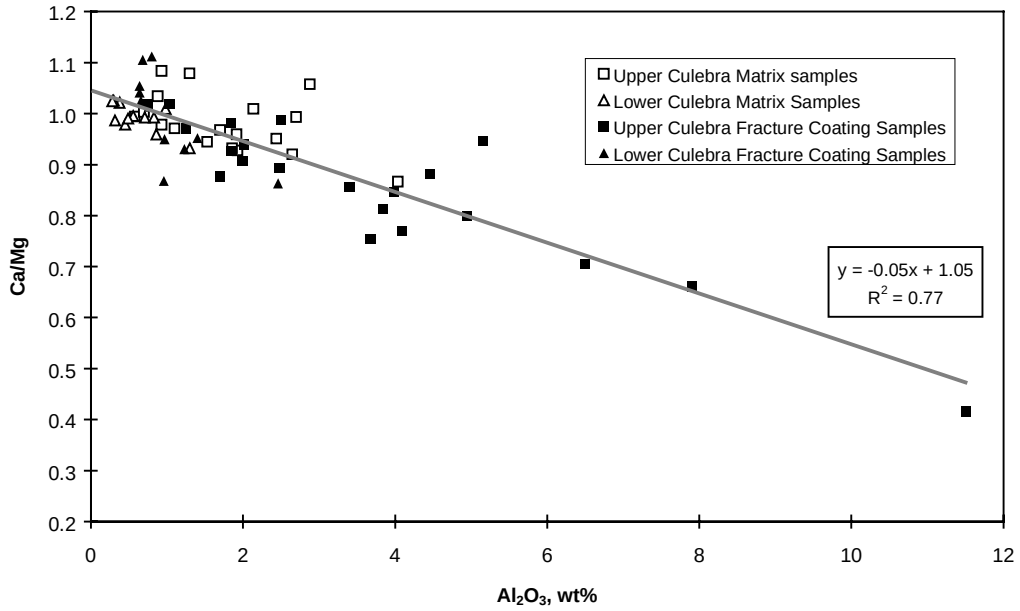

Figure 24. Ca/Mg vs. Al_2O_3 for coating and matrix samples. The Ca/Mg ratios have been corrected for gypsum using the measured SO_3 content of each sample. The y-axis intercept gives the Ca/Mg ratio of pure, clay-free dolomite in the Culebra.

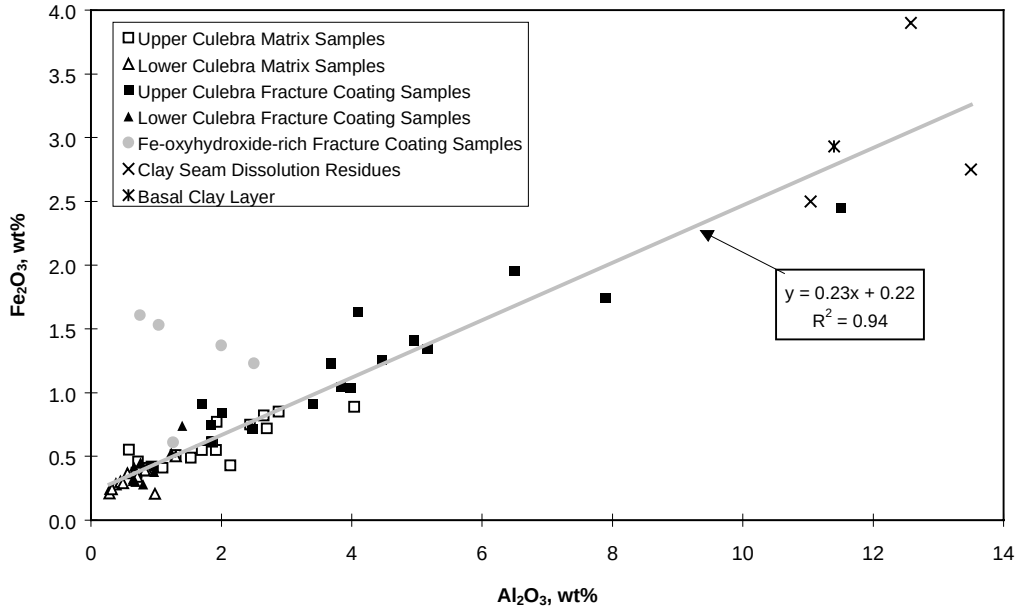

Figure 25. Measured Fe_2O_3 concentrations plotted against aluminum. Orange, Fe oxyhydroxide-rich fracture coating samples were not included in the linear regression. The y-axis intercept gives the Fe_2O_3* content of pure, clay-free dolomite in the Culebra.

As might be expected, samples from Fe-oxyhydroxide-rich fracture coatings are enriched in iron relative to the trend line, indicating that significant iron is present in minerals other than clays and dolomite.

3.4.4 Gypsum

Gypsum is a common vug- and fracture-filling material in the Culebra, and occasionally occurs as a cement in porous, silty dolomite. Gypsum-filled vugs and fractures commonly have clean, indistinct margins; however, selenite-filled fractures with clay selvages are also common.

A second sulfate phase, bassanite ($CaSO_4 \cdot \frac{1}{2}H_2O$), was identified in the bulk X-ray diffraction patterns of some samples. Bassanite was reported previously in the Culebra in Sewards et al. (1991c), who described it in thin sections from drill holes H-2, H-3 and H-4. They suggested that the bassanite may have been an artifact of sample processing, forming during thin section preparation. Citing Braitsch (1971) and Deer et al. (1962), they concluded that bassanite could not form by hydration of anhydrite or dehydration of gypsum under conditions likely to be present in the Culebra dolomite. Frictional heating during sample collection is a plausible origin for the bassanite detected in these samples, as the high-speed grinding tool became very hot during sampling.

3.4.5 Quartz

Quartz is a minor phase throughout the Culebra dolomite, occurring both disseminated throughout the dolomitic matrix and in clay-rich partings, and stringers, where the grains are commonly larger and present in higher concentrations than in the matrix. Euhedral authigenic grains and euhedral overgrowths on detrital grains are common. It is also common in clay-rich fracture coatings, but is not generally coarser than material occurring in the dolomitic matrix.

3.4.6 Halite

Halite was identified in several matrix and coating samples by XRD, and is inferred to be present in most samples from elevated chloride concentrations. In general, concentrations are higher in fracture coating samples than in matrix samples. Brines in the Culebra are undersaturated with respect to halite, so it is probable that the halite formed after core collection, by wicking and evaporation of pore water, and precipitation at the surface of the samples. As matrix samples were taken from directly beneath the fracture coating samples, they represent material that was not at the surface, and hence contained less precipitated halite.

3.4.7 Trace Minerals

Several other phases occur in minor amounts in the matrix and fracture coatings. Secondary or diagenetic phases include calcite, pyrite, potassium feldspar, a polymorph of TiO_2, and a possible zeolite. Detrital minerals include micas and several trace minerals resistant to weathering.

Calcite was not identified in the XRD patterns for any samples, but was identified during SEM imaging as a minor phase on some parting and fracture surfaces, where it presumably formed by

interaction with ground water. Sewards (1991) and Sewards et al. (1991a) found calcite in several samples of Culebra core, and suggested that it formed as a result of dedolomitization by meteoric water. The Ca/Mg ratios seen in the samples analyzed for this study (Figure 24), indicate that calcite is not a significant component in the Culebra.

Microscopic examination under reflected light of 20 polished petrographic thin sections from 9 different drill holes indicated that pyrite is a relatively common trace mineral in the Culebra dolomite. It occurs as irregular or framboidal masses up to 50 µm. Qualitatively, pyrite is somewhat more common in clay-rich layers and in clay-rich fracture coatings than in the dolomitic matrix.

Rare sub-to-anhedral grains of potassium feldspar were identified during microprobe analysis of polished thin sections. Krumhansl et al. (1990) found that diagenetic potassium feldspar in the Salado Formation contained subequal amounts of Na and K, indicating a monoclinic sanidine-like structure. However, microprobe analyses of feldspars in the Culebra show only potassium, and polysynthetic twinning in some grains indicates that the feldspar is triclinic.

One of the most common trace phases in the Culebra is a polymorph of titanium oxide. Though more abundant in clay-rich laminae, it is also disseminated throughout the dolomite matrix. It commonly occurs as euhedral grains less than 5 µm in diameter, but larger grains exhibiting a framboidal or skeletal habit are also present; suggesting that it is of diagenetic origin. Degradation of detrital biotite during diagenesis is one possible source of the titanium.

Euhedral, lath-like Ca, K aluminosilicates were observed on one parting surface (sample # 051090-28) during SEM imaging. These have been tentatively identified as zeolites.

Detrital muscovite and biotite are common phases in the Culebra dolomite, occurring as readily identifiable elongate grains in most petrographic thin sections. AEM analyses are given in Appendix D. Their distribution generally follows that of clay-rich laminae and seams, but they also occur as rare grains disseminated throughout the dolomite. Muscovite is the more common of the two. Detrital Fe-rich and Fe-poor chlorite were identified by Sewards et al. (1991a), but were not observed in this study.

Other, rarer detrital phases identified during AEM analysis include zircon, sphene, apatite, ilmenite, and monazite.

4. Discussion

The primary goal of this report is to examine the composition and distribution of clay minerals within the Culebra dolomite, and to determine if there is a concentration of clay minerals on surfaces within the unit which line potential conduits for groundwater flow. These issues can be examined on several scales. On a stratigraphic scale, it is necessary to document variations in the clay content and composition, and to determine if such variations have a lateral significance. On a smaller scale, we seek to determine if clays are concentrated on the fracture coatings, and to document any compositional differences between clays in the coatings and those in the underlying matrix. The EDTA dissolution results (Table 3) indicate that insoluble phases are consistently concentrated in surface coatings relative to the underlying matrix, and XRD analysis of the residues indicates that clays are present throughout the Culebra, and that the gross mineralogy is similar in all samples, in that the dominant clay minerals are corrensite and illite. However, these data do not give us precise information on the relative proportion of each clay mineral present, or on the overall amount of clay present.

4.1 Origin of Clays in the Culebra Dolomite

The clays found in the Culebra dolomite do not represent a detrital clay assemblage. Typical detrital clay assemblages contain dioctahedral smectites, illite, and interstratified illite/smectite (Bodine, 1985; Fisher, 1988). These detrital phases were diagenetically altered by interactions with Mg-rich brines to produce the corrensite, serpentine, and possibly some the chlorite present in the unit (Sewards et al., 1991a; Sewards et al., 1992), although large flakes of detrital chlorite were described by Sewards et al. (1991a,b).

Though illite was probably part of the original detrital clay assemblage, most or all of the illite present now is diagenetic. Rb-Sr age dating of fine clay fractions from the Culebra yielded Late Permian isochron ages, similar to the depositional age of the unit (Brookins et al., 1990). The other clays in the assemblage are notably K-poor (and, by inference, Rb-poor); individual clay crystallite analyses reported by Sewards et al. (1992) indicate that neither chlorite nor corrensite generally contain measurable K. Thus, the Rb-Sr age dates represent the age of the illite in the clay assemblage, and indicate that it formed diagenetically during or shortly after deposition of the unit.

The source of the clay in the clay-rich fracture coatings is not clear. As detrital grains of phyllosilicates and other resistant detrital trace minerals are commonly present in the coatings, the clays cannot have formed by direct precipitation onto the surface from the brines (the likely source of the Fe-oxyhydroxide coatings), or by reaction of the brines with the dolomitic wall rocks. It is possible that the clays and detrital mineral grains washed down from mudstones in the overlying Tamarisk member, but it seems unlikely that the clay mineral assemblage of the fracture coatings would so closely resemble that of the matrix if this were the case. Limited data in Sewards et al. (1992) suggest that the clay assemblage in the Tamarisk is somewhat more serpentine-rich than that of the Culebra. Also, it is not clear that large detrital mineral grains and fine-grained clays would be hydraulically similar enough to be transported and deposited together. Given the similarity in the mineralogy and composition of the clay assemblages on the fractures and in the matrix (see Figures 13 and 14), it seems probable that the fracture coatings are dissolution residues, formed *in situ* by dissolution of the dolomite matrix along the fracture walls.

4.2 Comparison of Culebra Clays with AIS-15 Clay

A black, clay-rich layer occurs in the lower member of the Rustler Formation, just below the Culebra Dolomite. This unit was sampled in the Air Intake Shaft at the WIPP site (sample AIS-15) and the clay-sized fraction of the sample was reported by Sewards et al. (1992) to be ~94% corrensite. Material from the black clay layer was used in several uranium adsorption studies, summarized in Park et al. (1995) and Prasad et al. (1998). Results of those studies indicated that this material, dominantly corrensite, has a high affinity for uranyl at pH values that are predicted to be important in radionuclide release scenarios from the WIPP repository (Figure 26).

The composition of the clays in AIS-15, as reported by Sewards et al. (1992), is plotted with those of the Culebra fine-grained clay mixtures in Figure 27. Although the AIS-15 sample contains more corrensite and less illite than the majority of the clays in the Culebra, it falls within the range of Culebra clay compositions measured in this study. It can be argued that the AIS-15 samples provide a good surrogate for Culebra clays in sorption studies, although on a gram per gram basis, the clays in the Culebra dolomite are probably less sorptive than the AIS-15 clay. The clay material from the black shale is 94% corrensite, and the average Culebra clay, 71% (Figure 15). Conservatively assuming that illite plays no role in sorption, then 1.0 gram of AIS-15 clay has a sorptive capacity equivalent to 0.94/0.71, or 1.35 grams, of Culebra clay.

4.2 Clay Concentrations per Unit Area on Fractures within the Culebra.

Estimates of the concentrations of clay present on each fracture surface can be made from the modal mineral compositions of the fracture coating and matrix samples. The calculations are described in Appendix E, and the results for each sample examined in this study are tabulated. They are summarized in Figure 28. Data have been grouped into high-angle (type A) and horizontal (types B and C) fractures. The clay seam data (type D) were not included. Within each grouping, depth from the top of the Culebra increases from left to right. Though the data are sparse and there is some scatter, a few generalizations can be made. Horizontal fractures are more consistently clay-rich than high-angle fractures, although high-angle fractures may also have substantial clay coatings. Also, in both groups, there is a weak correlation between clay content and stratigraphic height; samples from the top of the Culebra tend to have more clay on the fracture surfaces.

Data are too sparse for a strict statistical analysis of clay distributions on different surface types. The distribution of clay concentrations in the whole sample set is shown in Figure 29, along with a breakdown for high-angle and sub-horizontal fractures. The distribution is markedly non-normal, primarily due to a large number of fracture surfaces (mostly high-angle) with clay concentrations of 0–5 g/m^2. A log-normal distribution was fitted to the complete data set; the log-normal mean was 6.51 ± 5.25 g/m^2. Excluding the two samples with greater than 50 g/m^2 clay, that were associated with clay seams and were very local in extent, the log-normal mean was 5.1 ± 4.3 g/m^2. This might be considered a conservative estimate of the clay present *on fracture surfaces with visible coatings*, which Holt (1997) estimated comprised about 7% of the total fractures in Culebra core from drill hole H19b7.

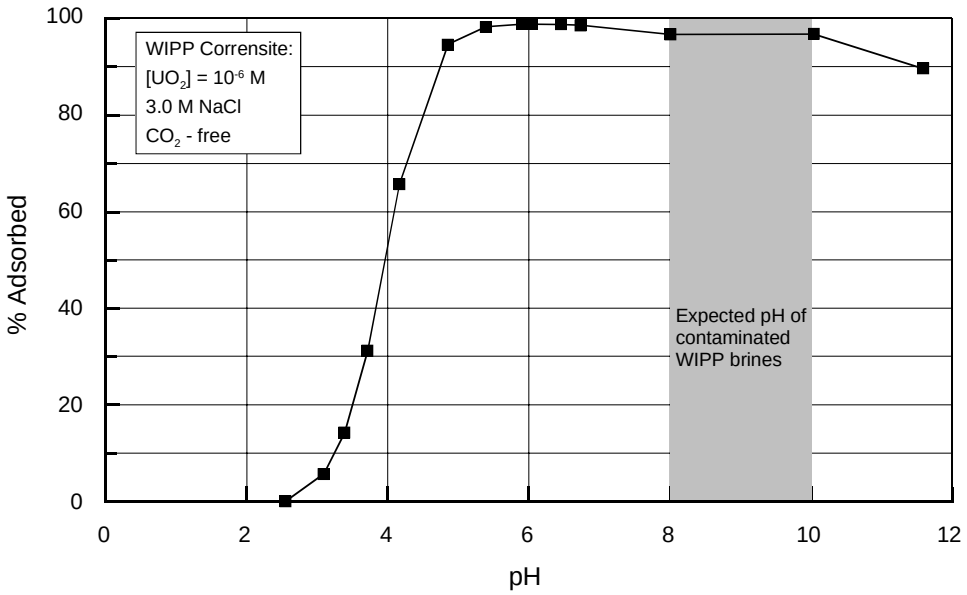

Figure 26. Adsorption of uranyl by material from samples AIS-15, which is dominantly corrensite. Data from Park et al. (1995).

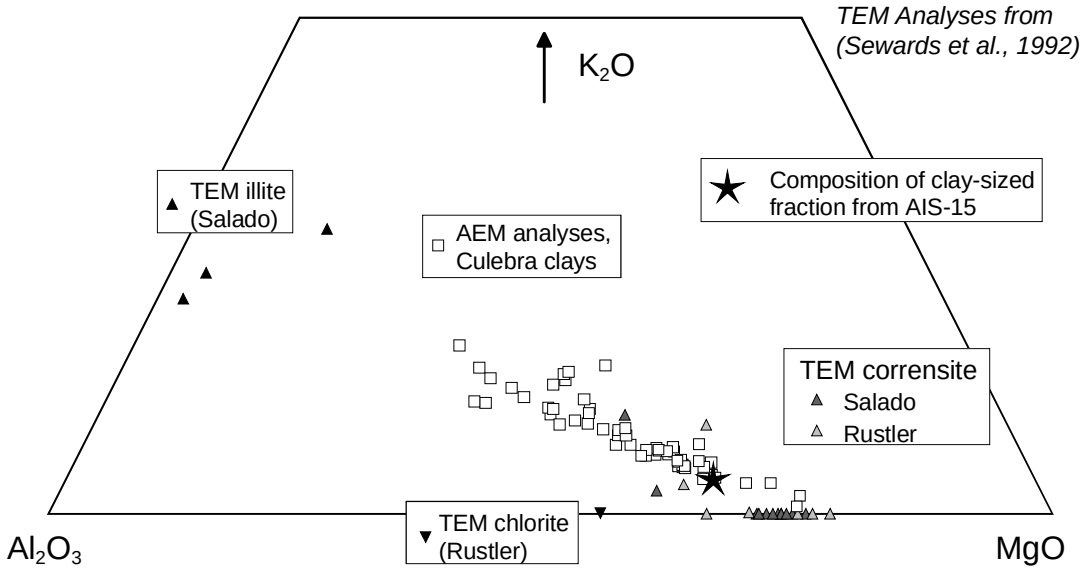

Figure 27. Composition of clay-sized material from the black clay layer in the lower member of the Rustler Formation, just below the Culebra (sample AIS-15). This clay has been used in several uranium adsorption studies.

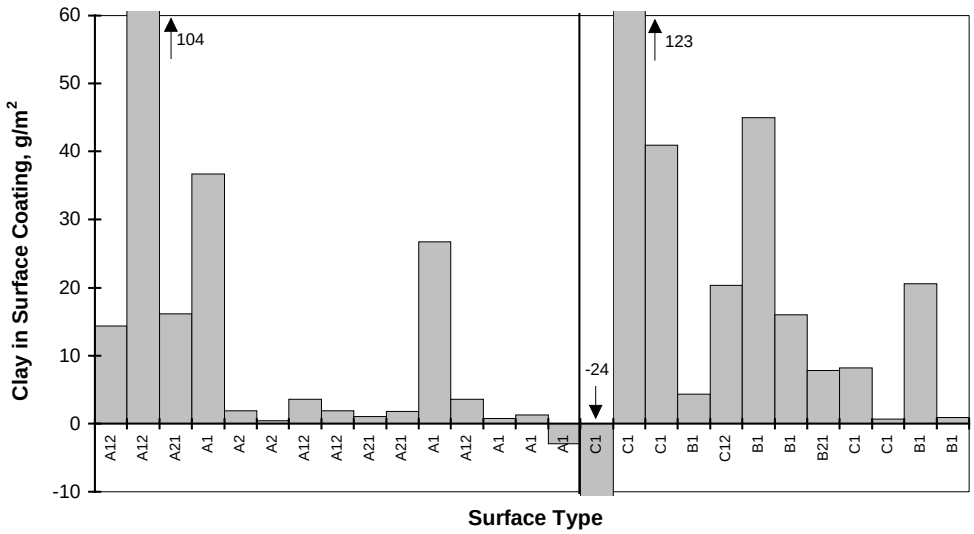

Figure 28. The amount of clay present per unit area on fracture surfaces in the Culebra. Estimated from the calculated modal clay contents of fracture coating and matrix samples.

4.3 The Effect of Fracture Coating Minerals and Matrix Clay on Radionuclide Transport Through the Culebra

Clay-rich fracture coatings in the Culebra are discontinuous and thin—commonly on the order of microns or 10's of microns thick. While such coatings appear to have a lower porosity than the underlying matrix material, it is unlikely that they significantly inhibit advective or diffusive transport across the fracture surface over time scales relevant to the WIPP site. Thus, the effect of the fracture coatings on hydrologic transport parameters is probably insignificant.

However, the coatings may be important with respect to geochemical transport. Although the volume of clay on the fracture surfaces per unit area is small, when integrated over the distances necessary to escape the WIPP site, the total amount of clay is large. Under the pH conditions predicted in WIPP brines, the distribution coefficients for uranyl adsorption onto corrensite are very high (Park et al., 1995). The experimental data shown in Figure 26 can be used to calculate a minimum K_d, over the pH range applicable to WIPP scenarios, of ~20,000 ml/g. Other transuranics are inferred to show similar behavior. Sorption K_ds measured for uranium onto crushed, sieved, and washed clay-poor Culebra dolomite, reported by Triay et al. (1998), are less than 10, while those on crushed clay-rich material (~60% clay), though varying with the CO_2 content of the simulated brine, are consistently higher, ranging up to 1000. It is likely that clay-rich fracture coatings, although thin and present on only a fraction of the total fracture surfaces, will contribute significantly to retardation of radionuclides in the Culebra.

Over time spans and transport distances relevant to WIPP radionuclide release scenarios, clays within the matrix of the Culebra will be accessed by advective/diffusive transport (Holt, 1997). Clay minerals, ~70% of which is corrensite, comprise 0.6% to perhaps 12% of the unit by weight—0.6% to 7% in the highly fractured lower part of the unit. The high measured K_ds for uranyl adsorption onto

Figure 29. Histograms of calculated clay concentrations, in grams/meter^2 on fracture coatings in the Culebra.

corrensite suggest that the clays will be an important phase in determining the adsorption properties of the Culebra matrix material.

Iron oxyhydroxides have been shown in numerous studies to have a strong affinity for uranium (Hsi and Langmuir, 1985; Yanase et al., 1991; Payne et al., 1994; Waite et al., 1994; Bruno et al., 1995), though none of these examined the behavior of uranium in a concentrated brine electrolyte. No attempt was made in this study to quantify the amount of Fe-oxyhydroxides present on fracture coatings in the Culebra, as such coatings are commonly very thin—no more than stains on the rock surface. Thus, it is not possible to evaluate the degree to which Fe-oxyhydroxide coatings will contribute to radionuclide retardation in the Culebra.

Intentionally Left Blank

5. Conclusions

The primary goal of this report is to examine the abundance, composition, and distribution of clay minerals from samples obtained in drill holes at several locations within the Culebra Dolomite in the vicinity of the WIPP site. Samples examined in this study were chosen because of the presence of open fractures, porous vug-rich zones, or visible fracture coatings, and thus are not representative of the entire population of fractures in the Culebra. Although not a quantitative, systematic, site-wide study of the frequency of occurrence of clay fracture coatings, this report provides a contribution to such a determination.

Clay minerals are present in the matrix and as fracture coatings in the samples from all the drill core locations examined in this study. Matrix clay concentrations vary from less than 1% to ~12%, and show a generally increasing trend with stratigraphic height in the unit. Clays occur disseminated throughout the dolomite matrix, and also as clay-rich laminae and partings that form both as primary sedimentary structures and as dissolution residues. Such partings are the loci of bedding plane fractures, and have the heaviest clay coatings found in the unit. Cross-cutting fractures also commonly exhibit clay mineral coatings, but these are generally discontinuous and much thinner. The matrix and fracture coating clay assemblages do not show any systematic mineralogical or compositional variation. Corrensite is the most abundant clay, comprising on the average about 70% of the total. Most of the remainder is illite, with minor chlorite and serpentine. The clays occur as mixtures of very fine-grained crystallites, and although the relative proportion of illite and corrensite in these mixtures is variable over distances of a few microns, there is no consistent difference between matrix and fracture coating samples, and no variation in the proportion with stratigraphic height. The amount of clay on the fracture surfaces averages 5.1 ± 4.3 grams of clay per square meter of fracture surface (lognormal mean and standard deviation) for the samples examined.

The clay mineralogy and published Rb-Sr isotopic data indicate that the present clay assemblage formed during or soon after deposition of the unit, by brine-induced diagenetic alteration of detrital clays. Clay coatings on horizontal fractures are probably depositional features. Similarities in the mineralogy and composition of the matrix and fracture coating clay assemblages suggest that the clay-rich coatings on high-angle fracture may be dissolution residues, formed *in situ* by dissolution of the dolomite matrix along the fracture walls. Iron oxyhydroxides are common on fractures throughout the unit. Microprobe analysis of Fe-rich fracture coatings and fracture fillings indicates that the coatings are stochiometrically FeOOH. Limited X-ray diffraction data indicate that some coatings are goethite, but variations in the color of the Fe-coated fractures suggests that other polymorphs of FeOOH may also be present. Pyrite (FeS_2) was commonly observed in the rock matrix.

The Compliance Certification Application (CCA) did not consider the potential effects of clay fracture skins on radionuclide transport. These potential effects include: 1) increased transport rates along advective flow paths due to inhibited advection/diffusion into the dolomite matrix, and 2) increased retardation due to sorption onto matrix-and fracture-coating clays. The information obtained in this study can support evaluation of alternative models for radionuclide retardation and provides a basis for selection of samples for laboratory-scale sorption and advection/diffusion experiments. Corrensite-rich

and Fe-oxyhydroxide-rich fracture coatings are probably too thin and discontinuous to affect large-scale, long-term advective/diffusive transport through the Culebra. However, numerous experimental studies have demonstrated the strong affinity of the clay minerals for uranium and other transuranic elements. This suggests that where locally abundant in the fracture and associated matrix, the clays could provide additional radionuclide sorption sites in the Culebra dolomite. Clay disseminated throughout the matrix of the dolomite, 0.6% to 12% by weight, could be accessed by advective/diffusive processes over time spans relevant to the WIPP site, and would affect the adsorption characteristics of the bulk rock.

The compositions of clays in the Culebra dolomite were compared to that of AIS-15, a well-characterized clay from the unnamed lower member of the Rustler Formation (Sewards et al., 1992; Park et al., 1995; Prasad et al., 1998) that used in sorption experiments. The similarity in composition suggests that the samples used in those mechanistic sorption studies are relevant to the prediction of radionuclide sorption by clays from the Culebra.

The occurrence of clay minerals and iron oxyhydroxides on the surfaces of open fractures, lining vugs, and disseminated in the matrix of the dolomite should be considered in evaluating the realism of K_ds distributions assumed for the Culebra in performance assessment. Such distributions will be conservative if they are based solely upon batch experiments using cleaned, clay-poor, coating-free material (Triay et al., 1998). In selecting samples for laboratory-scale advection/diffusion experiments, the presence of clay-rich fracture coatings and the distribution and concentration of clay in the dolomite matrix should be considered. In addition to affecting sorption K_ds, low permeability fracture coatings and clay-rich laminae may significantly inhibit advective/diffusive transport over the relatively short over times and distances used in laboratory-scale experiments. It should remembered that reactive tracer transport rates through even homogeneous rock samples probably vary with clay content, so extrapolations of experimental results to the field scale must be done with caution.

6. References

Beaufort, D., A. Baronnet, B. Lanson, and A. Meunier. 1997. "Corrensite: A Single Phase or a Mixed-Layer Phyllosilicate in the Saponite-to-Chlorite Conversion Series? A Case Study of Sancerre-Couy Deep Drill Hole (France)," *American Mineralogist*. Vol. 82, no. 1-2, 109-124.

Bodine, M.W., Jr. 1985. "Clay Mineralogy of Insoluble Residues in Marine Evaporites," *Mineralogy—Applications to the Minerals Industry, Proceedings of the Paul F. Kerr Memorial Symposium, New York, NY, February 28, 1985*. Eds. D.M. Hauser and O.C. Kopp. New York, NY: Society of Mining Engineers of the American Institute of Mining, Metallurgical, and Petroleum Engineers. 133-156.

Braitsch, O. 1971. *Salt Deposits, Their Origin and Composition*. Berlin; New York: Springer-Verlag.

Brookins, D.G., S.J. Lambert, and D.B. Ward. 1990. "Authigenic Clay Minerals in the Rustler Formation, WIPP Site Area, New Mexico," *Scientific Basis for Nuclear Waste Management XIII, Materials Research Society Symposium Proceedings, Boston, MA, November 27-30, 1989*. Eds. V.M. Oversby and P.W. Brown. SAND89-1405J. Pittsburgh, PA: Materials Research Society. Vol. 176, 665-672.

Bruno, J., J. de Pablo, L. Duro, and E. Figuerola. 1995. "Experimental Study and Modeling of the U(VI)-Fe$(OH)_3$ Surface Precipitation/Coprecipitation Equilibria," *Geochimica et Cosmochimica Acta*. Vol. 59, no. 20, 4113-4123.

Deer, W.A., R.A. Howie, and J. Zussman. 1962. *Rock-Forming Minerals. Volume 5: Non-Silicates*. London: Longmans; New York, NY: John Wiley & Sons.

Fisher, R.S. 1988. "Clay Minerals in Evaporite Host Rocks, Palo Duro Basin, Texas Panhandle," *Journal of Sedimentary Petrology*. Vol. 58, no. 5, 836-844.

Fu, L., K.L. Milliken, and J.M. Sharp, Jr. 1994. "Porosity and Permeability Variations in Fractured and Liesegang-banded Breathitt Sandstones (Middle Pennsylvanian), Eastern Kentucky: Diagenetic Controls and Implications for Modeling Dual-Porosity Systems," *Journal of Hydrology*. Vol. 154, nos. 1-4, 351-381.

Holt, R.M. 1997. *Conceptual Model for Transport Processes in the Culebra Dolomite Member, Rustler Formation*. SAND97-0194. Albuquerque, NM: Sandia National Laboratories.

Hsi, C.D., and D. Langmuir. 1985. "Adsorption of Uranyl onto Ferric Oxyhydroxides: Application of the Surface Complexation Site-Binding Model," *Geochimica et Cosmochimica Acta*. Vol. 49, no. 9, 1931-1941.

Krumhansl, J.L., K.M. Kimball, and C.L. Stein. 1990. *A Review of WIPP Repository Clays and Their Relationship to Clays of Adjacent Strata*. SAND90-0549. Albuquerque, NM: Sandia National Laboratories.

Moench, A.F. 1984. "Double-Porosity Models for a Fissured Groundwater Reservoir with Fracture Skin," *Water Resources Research*. Vol. 20, no. 7, 831-846.

Moench, A.F. 1995. "Convergent Radial Dispersion in a Double-Porosity Aquifer with Fracture Skin: Analytical Solution and Application to a Field Experiment in Fractured Chalk," *Water Resources Research.* Vol. 31, no. 8, 1823-1835.

Moore, D.M., and R.C. Reynolds, Jr. 1989. *X-Ray Diffraction and the Identification and Analysis of Clay Minerals*. New York, NY: Oxford University Press.

Park, S-W., J.O. Leckie, and M.D. Siegel. 1995. *Surface Complexation Modeling of Uranyl Adsorption on Corrensite from the Waste Isolation Pilot Plant Site: Preliminary Potentiometric and Uranyl Adsorption Measurements*. SAND90-7084. Albuquerque, NM: Sandia National Laboratories.

Payne, T.E., J.A. Davis, and T.D. Waite. 1994. "Uranium Retention by Weathered Schists – The Role of Iron Minerals," *Radiochimica Acta*. Vol. 66/67, 297-303.

Prasad, A., G. Redden, and J.O. Leckie. 1998. *Radionuclide Interactions at Mineral/Solution Interfaces in the WIPP Site Subsurface Environment*. Stanford University Report for Sandia National Laboratories, SNL Contract AG 4979. (Copy on file in the Sandia WIPP Central Files Sandia National Laboratories, Albuquerque, NM in WPO#43692).

Sewards, T. 1991. *Characterization of Fracture Surfaces in Dolomite Rock, Culebra Dolomite Member, Rustler Formation*. SAND90-7019. Albuquerque, NM: Sandia National Laboratories. 80 pp.

Sewards, T., R. Glenn, and K. Keil. 1991a. *Mineralogy of the Rustler Formation in the WIPP-19 Core*. SAND87-7036. Albuquerque, NM: Sandia National Laboratories. 90 pp.

Sewards, T., M.L. Williams, and K. Keil. 1991b. *Mineralogy of the Culebra Dolomite Member of the Rustler Formation*. SAND90-7008. Albuquerque, NM: Sandia National Laboratories. 135 pp.

Sewards, T., M.L. Williams, K. Keil, S.J. Lambert, and C.L. Stein. 1991c. "Mineralogy of the Culebra Dolomite," *Hydrogeochemical Studies of the Rustler Formation and Related Rocks in the Waste Isolation Pilot Plant Area, Southeastern New Mexico*. Eds. M.D. Siegel, S.J. Lambert, and K.L. Robinson. SAND88-0196. Albuquerque, NM: Sandia National Laboratories. 3-1 through 3-43.

Sewards, T., A. Brearley, R. Glenn, I.D.R. MacKinnon, and M.D. Siegel. 1992. *Nature and Genesis of Clay Minerals of the Rustler Formation in the Vicinity of the Waste Isolation Pilot Plant in Southeastern New Mexico*. SAND90-2569. Albuquerque, NM: Sandia National Laboratories. 46 pp.

Triay, I., D. Bish, S. Boone, S. Chipera, C. Cotter, C. Duffy, C. Mason, D. Vaniman, and R. Villareal. 1998. *Batch Sorption Data in Support of the Waste Isolation Pilot Plant Project.* Los Alamos National Laboratory Report for Sandia National Laboratories, SNL Contract AT 8745. (Copy on file in the Sandia WIPP Central Files Sandia National Laboratories, Albuquerque, NM in WPO#52655).

U.S. DOE (U.S. Depratment of Energy) 1996. *Title 40 CFR Part 191 Compliance Certification Application for the Waste Isolation Pilot Plant*. DOE/CAO-1996-2184. Carlsbad, NM: U.S. Department of Energy, Waste Isolation Pilot Plant, Carlsbad Area Office. Vols. I-XXI.

Waite, T.D., J.A. Davis, T.E. Payne, G.A. Waychunas, and N. Xu. 1994. "Uranium(VI) Adsorption to Ferrihydrite: Application of a Surface Complexation Model," *Geochimica et Cosmochimica Acta*. Vol. 58, no. 24, 5465-5478.

WIPP Analysis Plan AP-002. 1996. "Mineralogical and Chemical Analyses of Fracture, Matrix and Vug Lining Minerals in Selected Culebra Dolomite Samples Collected Prior to 1991." Revision 0, Effective Date 3/12/1996. Albuquerque, NM: Sandia National Laboratories. (Copy on file in the Sandia WIPP Central Files, Sandia National Laboratories, Albuquerque, NM as WPO#36349.)

WIPP Technical Operating Procedure TOP-543. 1996. "Operation of the Hitachi S-450 Scanning Electron Microscope for Analysis of Fracture Coatings on Culebra Dolomite Core and Hand Samples." Revision 0, Effective Date 3/14/96. Albuquerque, NM: Sandia National Laboratories. (Copy on file in the Sandia WIPP Central Files, Sandia National Laboratories, Albuquerque, NM as WPO#39515.)

WIPP Technical Operating Procedure TOP-552. 1996. "Calibration, Use and Maintenance of Philips XRG 3100 X-ray Generator." Revision 0, Effective Date 3/14/96. Albuquerque, NM: Sandia National Laboratories. (Copy on file in the Sandia WIPP Central Files, Sandia National Laboratories, Albuquerque, NM as WPO#39562.)

WIPP Technical Operating Procedure TOP-553. 1996. "Procedure for Bulk Chemical Analysis of Culebra Dolomite Fracture Coatings and Matrix Material." Revision 0, Effective Date 3/14/96. Albuquerque, NM: Sandia National Laboratories. (Copy on file in the Sandia WIPP Central Files, Sandia National Laboratories, Albuquerque, NM as WPO#39563.)

WIPP Technical Operating Procedure TOP-554. 1996. "Visual Description, Petrographic Description, Photography, and Sub-sampling of Clay-size Materials from Culebra Dolomite Samples." Revision 0, Effective Date 3/28/96. Albuquerque, NM: Sandia National Laboratories. (Copy on file in the Sandia WIPP Central Files, Sandia National Laboratories, Albuquerque, NM as WPO#39567.)

Yanase, N., T. Nightingale, T. Payne, and P. Duerden. 1991. "Uranium Distribution in Mineral Phases of Rock by Sequential Extraction Procedure," *Radiochimica Acta*. Vol. 52/53, 387-393.

Intentionally Left Blank

Appendix A. Chemical Analyses

Samples were completely digested with hydrofluoric and nitric acids, and the 10 major elements, chlorine and sulfur were analyzed using wet chemical methods. The bulk of the elements were analyzed by atomic absorption; for larger samples, SiO_2 was measured using a more accurate gravimetric method. P_2O_5 and SO_3 were determined photometrically, using colorimetric and turbidometric methods, respectively. Chloride was determined by ion chromatography. H_2O^- and (H_2O^+ + CO_2) were determined gravimetrically, by weight loss at 110 and 1000º C, respectively. Analytical variability was determined from calibration standards run with the samples, and is ±3% for elements present in concentrations greater than 1%, ±10% for elements present in concentrations of 1.0–0.1%, and ±20% for elements reported at concentrations of <0.1%. Due to the small sample sizes and the inherent imprecisions in the methods used, reported SiO_2 and SO_3 values are ±10%. Several samples yielded poor totals, outside of the normally accepted range of 97–102%. This is mostly a function of the small sample sizes, which made accurate gravimetric determinations difficult. Also, during ignition, some or all chlorine was driven off and chloride-bound cations became oxides, causing a weight gain that offset the loss of H_2O and CO_2 and resulted in poor totals. Oxidation of reduced organic matter may have had a similar affect. As a result, errors in the (H_2O^+ + CO_2) values are large, perhaps as great as ±25%. For samples with poor totals, the least reliable numbers are given in parentheses.

Table A-1. Compositional data for Culebra fracture coatings and matrix material.

Depth, ft	Sample ID	SiO_2	TiO_2	Al_2O_3	Fe_2O_3*	MnO	MgO	CaO	Na_2O	K_2O	P_2O_5	SO_3	H_2O^-	H_2O^++CO	Cl^-	Total
								Drill hole H2b								
632.0	**051190-107**															
	Coating	(31.77)	0.18	3.98	1.04	0.018	17.90	21.05	0.16	1.26	0.047	---	0.93	(37.35)	---	115.69
	Matrix	10.10	0.10	2.70	0.72	0.015	18.90	26.25	0.11	0.81	0.031	0.20	0.16	40.42	0.10	100.61
637.0	**051190-109**															
	Coating	(12.46)	<0.09	1.23	0.53	0.017	20.00	27.85	0.09	0.34	0.021	2.80	0.30	(42.28)	0.55	108.47
	Matrix	2.71	<0.09	0.83	0.39	0.015	20.70	29.30	0.06	0.23	0.019	1.04	0.70	43.98	0.10	100.07
								Drill hole H14								
547.9	**051190-59**															
	Coating	24.90	0.21	5.16	1.34	0.025	12.60	16.60	0.34	1.92	0.072	<0.17	0.00	29.28	---	92.45
	Matrix	(0.35)	<0.05	2.88	0.85	0.026	15.80	23.25	0.16	1.06	0.040	<0.17	0.13	36.77	---	81.32
553.4	**051190-61**															
	Clay seam	21.17	0.18	4.95	1.41	0.021	17.80	19.96	0.19	1.28	0.050	0.28	0.18	32.79	0.15	100.41
	Matrix	6.53	<0.09	1.93	0.77	0.018	20.40	26.65	0.11	0.53	0.023	0.46	0.33	42.20	0.13	100.08

Table A-1. Continued.

Depth, ft	Sample ID	SiO_2	TiO_2	Al_2O_3	Fe_2O_3*	MnO	MgO	CaO	Na_2O	K_2O	P_2O_5	SO_3	H_2O^-	H_2O^++CO	Cl^-	Total
								Drill hole H14, continued								
554.0	**051190-62**															
	Coating 1	8.93	<0.18	2.00	1.37	0.015	19.20	25.10	0.09	0.36	0.022	1.28	0.80	40.60	0.40	100.17
	Coating 2	11.22	0.14	2.01	0.84	0.016	16.80	25.85	0.10	0.55	0.030	5.59	1.50	35.07	0.26	99.98
	Matrix	7.83	0.09	1.70	0.55	0.014	18.80	26.70	0.09	0.46	0.022	1.99	0.48	40.55	0.15	99.42
								Drill hole H15								
870.5	**051090-22**															
	Coating	15.10	0.15	3.84	1.05	0.017	16.70	19.00	5.25	1.15	0.046	0.20	0.54	43.30	---	106.34
	Matrix	4.44	0.06	2.14	0.43	0.015	19.80	27.80	0.15	0.37	0.026	<.17	0.30	45.42	---	100.95
879.8	**051090-26**															
	Coating	5.70	0.08	0.96	0.42	0.013	14.70	22.65	8.70	0.29	0.028	7.00	1.23	(50.54)	---	112.31
	Matrix	4.50	0.09	0.86	0.39	0.014	15.50	26.50	3.50	0.23	0.028	8.30	2.04	43.73	---	105.68
877.7	**051090-28**															
	Coating	12.55	0.14	2.46	0.75	0.015	19.20	23.20	3.70	0.56	0.068	0.20	0.27	43.35	---	106.46
	Matrix	2.14	<0.05	0.38	0.28	0.014	20.40	29.10	0.24	0.10	0.017	0.17	0.43	46.12	---	99.39
								Drill hole H16								
705.0	**051190-80**															
	Coating	19.56	0.18	4.46	1.26	0.020	15.50	19.50	1.57	1.48	0.072	0.67	0.00	32.91	---	97.18
	Clay seam	49.52	0.52	11.50	2.45	0.028	9.70	5.60	0.69	4.60	0.165	<.17	0.60	13.96	---	99.33
	Matrix	8.00	0.08	1.92	0.55	0.018	19.20	25.80	0.25	0.75	0.034	0.25	0.16	42.70	---	99.71
	Seam, EDTA	60.18	0.76	13.50	2.75	0.024	8.18	0.12	0.66	5.50	0.083	<0.02	0.45	5.43	0.01	97.63
708.0	**051190-82**															
	Coating	(14.34)	<0.09	1.85	0.75	0.018	19.10	25.40	1.78	0.61	0.027	1.10	<0.1	(41.24)	1.67	107.89
	Matrix	4.30	<0.09	1.53	0.49	0.017	21.30	28.25	0.34	0.49	0.023	0.37	0.42	43.55	0.31	101.39
704.8	**051190-83**															
	Coating	35.06	0.34	7.90	1.74	0.023	12.60	11.60	0.78	3.00	0.120	<.17	0.00	22.64	---	95.80
	Matrix	11.28	0.10	2.44	0.75	0.022	18.30	24.20	0.24	0.93	0.040	<.17	0.03	40.08	---	98.41
713.2	**051190-84**															
	Coating	7.42	0.24	3.68	1.23	0.020	16.00	19.60	1.61	1.08	0.050	4.00	0.00	36.12	---	91.05
	Matrix	4.85	0.08	0.88	0.41	0.016	19.60	28.20	0.22	0.27	0.013	<.17	0.45	44.79	---	99.78
718.1	**051190-86**															
	Coating	6.10	<0.18	1.40	0.74	0.019	15.70	20.80	1.56	0.03	0.024	--	<0.1	49.60	---	95.97
	Matrix	6.63	<0.09	1.30	0.50	0.024	20.90	27.25	0.40	0.27	0.030	0.22	<0.1	43.21	0.31	101.04

Table A-1. Continued.

Depth, ft	Sample ID	SiO_2	TiO_2	Al_2O_3	Fe_2O_3*	MnO	MgO	CaO	Na_2O	K_2O	P_2O_5	SO_3	H_2O^- H_2O^++CO	Cl^-	Total
							Drill hole H18								
692.9	**051090-44**														
	Coating	25.03	0.20	6.50	1.95	0.024	16.00	16.65	0.36	1.93	0.072	1.39	0.74	28.40	0.24	99.48
	Matrix	9.95	0.01	2.65	0.82	0.020	19.30	25.05	0.15	0.80	0.036	0.50	0.20	40.27	0.09	99.85
694.2	**051090-47**														
	Coating	14.72	0.22	2.50	1.23	0.018	11.40	24.30	0.21	0.80	0.043	12.32	4.30	25.82	0.18	98.06
	Matrix	4.22	<0.09	0.93	0.42	0.016	16.80	29.80	0.09	0.16	0.023	6.39	1.62	38.52	0.10	99.09
695.7	**051090-48**														
	Coating	17.03	0.10	4.09	1.63	0.023	13.20	21.15	0.23	1.23	0.058	10.00	0.34	30.24	---	99.32
	Matrix	6.00	0.05	1.30	0.51	0.018	17.80	28.00	0.08	0.42	0.023	1.83	0.53	41.72	---	98.28
696.9	**051090-46**														
	Coating	5.73	<0.18	1.26	0.61	0.017	19.70	26.60	0.15	0.14	0.007	---	1.80	43.00	---	99.01
	Matrix	4.07	<0.09	1.10	0.41	0.016	21.10	28.95	0.14	0.33	0.021	0.64	<0.10	44.06	0.20	101.04
							Drill hole WIPP-19								
770.1	**051190-119**														
	Coating	5.06	<0.05	0.80	0.28	0.010	10.60	16.40	20.00	0.23	0.020	<0.17	0.00	(64.78)	---	118.18
	Matrix	1.70	0.10	0.30	0.25	0.013	20.40	29.10	0.61	0.10	0.011	<0.17	0.19	47.37	---	100.14
	Mtx, silty dolo	1.58	<0.05	0.29	0.21	0.016	20.20	28.80	0.43	0.16	0.010	<0.17	0.26	47.15	---	99.10
							WIPP Exhaust Shaft								
720.0	**051190-95**														
	Coating	4.84	<.05	1.04	1.53	0.019	14.90	23.00	8.80	0.36	0.028	2.70	0.44	(52.04)	---	109.70
	Matrix	3.02	<.05	0.72	0.46	0.017	19.80	28.00	1.26	0.26	0.020	<.17	0.38	46.99	---	100.93
721.0	**ESM-147**														
	Coating	(15.78)	0.10	1.70	0.91	0.013	14.20	(19.00)	(13.10)	0.39	0.028	2.41	0.20	(39.54)	(15.16)	122.53
	Matrix	3.86	<0.09	0.93	0.40	0.014	20.80	28.80	1.90	0.25	0.022	0.71	0.12	44.33	1.95	104.09
ESM161372-woclt250u															
	Shale layer	45.90	0.42	11.40	2.93	0.027	14.30	2.00	1.84	2.00	0.140	2.93	3.89	16.56	---	104.34
							Drill hole H19b7								
742.85	**H19b7-742.85**														
	Coating	13.40	0.18	3.40	0.91	0.016	13.60	20.70	3.85	1.35	0.052	6.41	2.39	29.27	4.36	99.88
	Matrix	14.23	0.12	4.04	0.89	0.017	14.20	21.30	0.98	1.75	0.062	5.97	1.57	31.59	0.85	97.56
744.6	**H19b7-744.6**														
	Coating	11.75	0.10	2.48	0.72	0.017	18.20	23.20	1.76	0.91	0.024	0.80	0.44	38.11	2.00	100.50
	Matrix	8.75	0.08	1.86	0.61	0.015	18.80	24.90	1.25	0.68	0.022	0.75	0.33	40.06	1.46	99.57
	Coating,	65.99	0.66	11.04	2.50	0.022	6.44	0.23	0.47	4.45	0.010	<0.02	0.34	4.30	0.08	96.52

Table A-1. Continued.

Depth, ft	Sample ID	SiO_2	TiO_2	Al_2O_3	Fe_2O_3*	MnO	MgO	CaO	Na_2O	K_2O	P_2O_5	SO_3	H_2O^- H_2O^++CO	Cl^-	Total
							Drill hole H19b7, continued								
752.0	**H19b7-752.0**														
	Coating	2.84	<0.14	0.75	1.61	0.013	13.30	22.00	10.26	0.25	0.030	4.50	1.69	38.29	12.26	107.79
	Matrix	2.39	<0.07	0.58	0.55	0.012	19.10	27.10	2.02	0.18	0.013	0.99	4.21	40.16	2.50	99.80
752.2	**H19b7-752.2**														
	Coating	8.85	0.12	1.84	0.61	0.014	17.20	24.30	2.88	0.54	0.036	1.17	0.49	39.61	3.00	100.67
	Matrix	2.94	0.08	0.70	0.37	0.013	19.20	27.30	1.71	0.23	0.013	0.73	0.52	43.45	1.98	99.24
754.7	**H19b7-754.7**														
	Coating	2.16	<0.14	0.66	0.42	0.013	19.48	28.12	2.52	0.19	0.024	0.48	0.00	44.37	2.80	101.23
	Matrix	1.54	0.09	0.32	0.24	0.011	21.00	28.90	1.18	0.13	0.008	0.12	0.29	45.26	1.41	100.50
755.0	**H19b7-755.0**														
	Coating	1.76	0.12	0.76	0.45	0.012	18.90	27.00	3.69	0.25	0.016	0.49	0.03	43.73	3.99	101.20
	Matrix	2.75	0.08	0.56	0.37	0.011	20.80	28.90	1.46	0.19	0.010	0.14	0.01	44.51	1.66	101.44
	Mtx, powdery	3.24	0.08	0.71	0.34	0.016	20.90	28.90	0.30	0.22	0.015	0.05	0.10	45.28	0.30	100.45
757.6	**H19b7-757.6**														
	Coating	4.61	0.08	0.97	0.38	0.014	19.90	26.40	1.26	0.33	0.031	0.15	0.11	44.34	1.24	99.81
	Matrix	2.12	<0.07	0.45	0.30	0.011	21.10	28.80	0.91	0.16	0.120	0.11	0.06	45.51	1.01	100.66
758.7	**H19b7-758.7**														
	Coating 1	2.57	<0.14	0.64	0.31	0.012	16.96	25.56	6.38	0.16	0.008	1.42	0.81	44.14	6.67	105.64
	Coating 2	2.91	<0.07	0.64	0.32	0.015	18.26	27.00	4.36	0.19	0.010	0.32	0.24	44.35	4.65	103.25
	Matrix	2.02	0.11	0.49	0.29	0.011	19.80	27.50	2.29	0.15	0.001	0.32	0.17	45.21	2.82	101.18
761.8	**H19b7-761.8**														
	Coating	3.08	<0.14	0.68	0.30	0.011	13.60	29.60	5.40	0.16	0.016	12.39	3.31	33.41	6.50	108.46
	Matrix	1.94	<0.07	0.98	0.21	0.010	12.10	29.20	1.50	0.11	0.012	17.44	4.21	30.77	1.76	100.24

Appendix B. Mineral Identification by X-Ray Diffraction

The following tables contain listings of the mineral phases identified by XRD in each sample. It should be noted that peak height is a measure of the diffracting power of a mineral phase, not a direct measure of abundance. Well-crystallized materials such as quartz or dolomite will have prominent peaks even if present in minor amounts, while poorly-crystalline clays will produce small peaks even if they are the dominant phase present in the sample.

—	= Not detected	X	= Small peaks
tr	= trace	XX	= Medium peaks
		XXX	= Large peaks

Table B-1. XRD Mineral Identification

Depth, ft	Sample ID	Corrensite	Illite	Chlorite	Serpentine	Quartz	Dolomite	Gypsum	Halite	Goethite
					Drill hole H2b					
632.0	**051190-107**									
	Coating	—	—	tr	—	X	XXX	—	—	—
	Matrix, EDTA res.	X	X	X	tr?	XXX	—	—	—	—
637.0	**051190-109**									
	Coating	tr	tr	—	—	X	XXX	X	—	—
	Coating, EDTA res.	tr	X	X	—	XXX	tr	—	—	—
	Matrix, EDTA res.	X	X	X	—	XXX	—	—	—	—
					Drill hole H14					
547.9	**051190-59**									
	Coating	tr	X	tr	—	XX	XXX	tr[†]	—	—
	Matrix	tr	tr	tr	—	XX	XXX	tr[†]	—	—
	Coating, EDTA res.	XX	XX	XX	—	XXX	—	—	—	—
	Matrix, EDTA res.	X	X	X	—	XXX	—	—	—	—
553.4	**051190-61**									
	Coating	—	tr	—	—	XX	XXX	X	—	—
	Matrix, EDTA res.	XX	X	X	—	XXX	—	—	—	—
554.0	**051190-62**									
	Coating	tr	tr	tr	—	XX	XXX	tr	X	—
	Matrix, EDTA res.	XX	X	X	—	XXX	—	—	—	—

[†] Bassanite

Table B-1. Continued.

Depth, ft	Sample ID	Corrensite	Illite	Chlorite	Serpentine	Quartz	Dolomite	Gypsum	Halite	Goethite
					Drill hole H15					
870.5	**051090-22**									
	Coating	tr	tr	tr	—	XX	XXX	—	XX	—
	Matrix	tr	—	—	—	X	XXX	—	—	—
	Coating, EDTA res.	XX	X	X	tr?	XXX	—	—	—	—
	Matrix, EDTA res.	XX	XX	XX	—	XXX	—	—	—	—
879.8	**051090-26**									
	Coating	—	—	—	—	X	XXX	X	XX	—
	Matrix	—	—	—	—	X	XXX	X[†]	XX	—
	Coating, EDTA res.	X	X	X	—	XXX	—	—	—	—
	Matrix, EDTA res.	X	X	X	—	XXX	—	—	—	—
877.7	**051090-28**									
	Coating	tr	tr	—	—	X	XXX	tr	X	—
	Matrix	—	—	—	—	X	XXX	X	X	—
	Coating, EDTA res.	XX	X	X	tr	XXX	—	—	—	—
	Matrix, EDTA res.	X	X	X	—	XXX	—	—	—	—
					Drill hole H16					
705.0	**051190-80**									
	Fracture Coating	tr	tr	tr	—	XX	XXX	tr	X	—
	Matrix	—	—	—	—	XX	XXX	—	—	—
	Clay Seam	X	X	X	—	XXX	XX	—	tr	—
	Coating, EDTA res.	XXX	XX	X	—	XXX	—	—	—	—
	Seam, EDTA res.	XX	X	X	tr	XXX	—	—	—	—
708.0	**051190-82**									
	Coating	—	tr	—	—	XX	XXX	—	X	—
	Coating, EDTA res.	—	tr	—	—	XXX	—	—	—	—
	Matrix, EDTA res.	X	X	X	—	XXX	X	—	—	—
704.8	**051190-83**									
	Coating	tr	tr	tr	—	XX	XXX	—	X	—
	Matrix	—	—	—	—	XX	XXX	—	—	—
	Coating, EDTA res.	XX	XX	X	—	XXX	—	—	—	—
	Matrix, EDTA res.	X	X	X	—	XXX	—	—	—	—

[†] tr. Bassanite

Table B-1. Continued.

Depth, ft	Sample ID	Corrensite	Illite	Chlorite	Serpentine	Quartz	Dolomite	Gypsum	Halite	Goethite
					Drill hole H16, continued					
713.2	**051190-84**									
	Coating	tr	tr	tr	—	XX	XXX	tr	X	—
	Matrix	—	—	—	—	X	XXX	tr	—	—
	Matrix, EDTA res.	X	X	X	tr	XXX	—	—	—	—
718.1	**051190-86**									
	Matrix, EDTA res.	XX	X	X	tr	XXX	—	—	—	—
					Drill hole H18					
692.9	**051090-44**									
	Coating, EDTA res.	XXX	XX	X	—	XXX	—	—	—	—
	Matrix, EDTA res.	X	X	X	—	XXX	—	—	—	—
696.9	**051090-46**									
	Coating, EDTA res.	X	X	X	—	XXX	—	—	—	—
	Matrix, EDTA res.	X	X	X	—	XXX	tr	—	—	—
694.2	**051090-47**									
	Coating	—	tr	—	—	XX	XXX	XX	—	—
	Coating, EDTA res.	X	X	X	—	XXX	tr	—	—	—
	Matrix, EDTA res.	XXX	X	X	tr	XXX	—	—	—	—
695.7	**051090-48**									
	Coating	tr	tr	tr	—	XX	XXX	XX[†]	X	—
	Matrix	—	—	tr	—	X	XXX	tr[†]	X	—
	Coating, EDTA res.	XX	XX	XX	—	XXX	—	—	—	—
	Matrix, EDTA res.	X	X	X	—	XXX	—	—	—	—
					Drill hole WIPP-19					
770.1	**051190-119**									
	Coating	—	—	—	—	X	XXX	—	XXX	—
	Mtx (2), silty dolo.	—	—	—	—	X	XXX	—	tr	—
	Mtx (2), EDTA res.	X	X	X	—	XXX	—	—	—	—
					WIPP Exhaust Shaft					
720.0	**051190-95**									
	Coating	tr	—	—	—	X	XXX	X	XX	—
	Matrix	tr	tr	tr	—	X	XXX	—	X	—
	Coating, EDTA res.	X	X	tr	—	XXX	—	—	—	—
	Matrix, EDTA res.	X	X	X	—	XXX	—	—	—	—

[†] Bassanite

Table B-1. Continued.

Depth, ft	Sample ID	Corrensite	Illite	Chlorite	Serpentine	Quartz	Dolomite	Gypsum	Halite	Goethite
					WIPP Exhaust Xhaft. continued					
721.0	**ESM-147**									
	Coating	—	—	—	—	X	XXX	tr	XXX	—
	Coating, EDTA res.	X	XX	X	—	XXX	—	—	—	—
	Matrix, EDTA res.	X	X	X	tr	XXX	—	—	—	—
					Drill hole H19b7					
742.85	**H19b7-742.85**									
	Coating	tr	tr	tr	—	XX	XXX	X	XX	—
	Coating, EDTA res.	X	X	X	—	XXX	—	—	—	—
	Matrix, EDTA res.	X	X	X	tr	XXX	—	—	—	—
744.6	**H19b7-744.6**									
	Coating	tr	tr	tr	—	XX	XXX	X	XX	—
	Coating, EDTA res.	X	X	X	—	XXX	—	—	—	—
	Matrix, EDTA res.	X	X	X	tr	XXX	—	—	—	—
752.0	**H19b7-752.0**									
	Coating	—	—	—	—	X	XXX	XX	XX	—
	Coating, EDTA res.	X	X	X	—	XXX	—	—	—	—
	Matrix, EDTA res.	X	X	X	—	XXX	—	—	—	—
752.2	**H19b7-752.2**									
	Coating	—	tr	tr	—	X	XXX	X	XX	—
	Coating, EDTA res.	X	X	X	—	XXX	—	—	—	—
	Matrix, EDTA res.	X	X	X	—	XXX	—	—	—	—
754.7	**H19b7-754.7**									
	Coating	—	—	—	—	XX	XXX	tr	tr	—
	Coating, EDTA res.	XX	X	X	—	XXX	—	—	—	—
	Matrix, EDTA res.	tr	tr	tr	—	XXX	—	—	—	—
755.0	**H19b7-755.0**									
	Coating	tr	tr	—	—	XX	XXX	tr	XX	—
	Coating, EDTA res.	X	X	X	—	XXX	—	—	—	—
	Mtx (1), EDTA res.	X	X	X	—	XXX	—	—	—	—
	Mtx (2), EDTA res.	X	X	X	—	XXX	—	—	—	—
757.6	**H19b7-757.6**									
	Coating	—	tr	—	—	X	XXX	tr	X	—
	Coating, EDTA res.	XX	X	X	—	XXX	—	—	—	—
	Matrix, EDTA res.	X	X	X	—	XXX	—	—	—	—

Table B-1. Continued

Depth, ft	Sample ID	Corrensite	Illite	Chlorite	Serpentine	Quartz	Dolomite	Gypsum	Halite	Goethite
					Drill hole H19b7, continued					
758.7	**H19b7-758.7**									
	Coating (1)	—	—	—	—	XX	XXX	X	XX	—
	Coating (2)	—	—	—	—	XX	XXX	X	XX	—
	Coat. (2), EDTA res.	X	X	X	—	XXX	—	—	—	—
	Matrix, EDTA res.	XX	X	X	—	XXX	—	—	—	—
761.8	**H19b7-761.8**									
	Coating	—	—	—	—	X	XXX	XX	XX	—
	Matrix, EDTA res. *	X	tr	tr	—	XXX	—	—	—	—

* Very poor pattern

Intentionally Left Blank

Appendix C. Modal Analyses

Whole rock modal mineral compositions were calculated as described in Sewards et al. (1991a), using the bulk mineral compositions listed in Appendix A. Totals commonly fall between 90% and 110%, suggesting that this method is accurate to about ±10 %. Surface types (see Figure 3) are listed for reference.

Table C-1. Modal Mineral Compositions

Depth, ft	Sample ID	Type	Clay	Quartz	Gypsum	Dolomite	Halite	Total
			Drill hole H2b					
632.0	**051190-107**							
	Coating	C12	26.53	19.56	0.00	0.08	69.24	115.43
	Matrix		18.00	1.82	0.43	0.06	85.89	106.20
637.0	**051190-109**							
	Coating	B21	8.20	8.69	6.02	0.05	85.15	108.11
	Matrix		5.53	0.16	2.24	0.03	94.98	101.95
			Drill hole H14					
547.9	**051190-59**							
	Coating	C1	34.40	9.08	0.00	0.18	54.61	98.26
	Matrix		19.20	-8.48	0.00	0.08	76.48	87.28
553.4	**051190-61**							
	Clay seam	D1	33.00	5.99	0.60	0.10	65.01	104.71
	Matrix		12.87	0.61	0.99	0.06	86.60	101.13
554.0	**051190-62**							
	Coating 1	A21	13.33	2.80	2.75	0.05	79.61	98.54
	Coating 2	A12	13.40	5.06	12.02	0.05	72.14	102.67
	Matrix		11.33	2.62	4.28	0.05	83.24	101.52
			Drill hole H15					
870.5	**051090-22**							
	Coating	B1	25.60	3.32	0.43	2.78	62.04	94.18
	Matrix		14.27	-2.12	0.00	0.08	91.45	103.67
879.8	**051090-26**							
	Coating	B1	6.40	2.76	15.05	4.61	58.36	87.19
	Matrix		5.73	1.86	17.85	1.86	68.03	95.33
877.7	**051090-28**							
	Coating	B1	16.40	5.01	0.43	1.96	75.85	99.65
	Matrix		2.53	0.97	0.37	0.13	95.33	99.33
			Drill hole H16					
705.0	**051190-80**							
	Coating	A12	29.73	5.88	1.44	0.83	62.60	100.49
	Clay seam	D1	76.67	14.25	0.00	0.37	18.42	109.71
	Matrix		12.80	2.11	0.54	0.13	84.29	99.87
	Seam, EDTA res.		90.00	18.78	0.00	0.35	0.39	109.52
708.0	**051190-82**							
	Coating	B1	12.33	8.67	2.37	0.94	81.02	105.33
	Matrix		10.20	-0.39	0.80	0.18	92.07	102.86

Table C-1. Continued.

Depth, ft	Sample ID	Type	Clay	Quartz	Gypsum	Dolomit	Halite	Total
			Drill hole H16					
704.8	**051190-83**							
	Coating	C1	52.67	10.83	0.00	0.41	38.16	102.07
	Matrix		16.27	3.80	0.00	0.13	79.61	99.80
713.2	**051190-84**							
	Coating	B1	24.53	-3.87	8.60	0.85	55.25	85.37
	Matrix		5.87	2.15	0.00	0.12	92.76	100.90
718.1	**051190-86**							
	Coating	C1	9.33	1.81	0.00	0.83	68.42	80.39
	Matrix		8.67	2.64	0.47	0.21	89.13	101.13
			Drill hole H18					
692.9	**051090-44**							
	Coating	A12	43.33	5.10	2.99	0.19	51.56	103.17
	Matrix		17.67	1.82	1.08	0.08	81.25	101.89
696.9	**051090-46**							
	Coating	A2	8.40	1.87	0.00	0.08	87.50	97.85
	Matrix		7.33	0.70	1.38	0.07	93.75	103.23
694.2	**051090-47**							
	Coating	A21	16.67	7.05	26.49	0.11	51.52	101.85
	Matrix		6.20	1.37	13.74	0.05	83.29	104.65
695.7	**051090-48**							
	Coating	A1	27.27	4.49	21.51	0.12	46.51	99.89
	Matrix		8.67	2.01	3.94	0.04	87.88	102.54
			Drill hole WIPP-19					
770.1	**051190-119**							
	Coating	C1	5.33	2.61	0.00	10.60	53.95	72.49
	Matrix		2.00	0.78	0.00	0.32	95.72	98.83
	Matrix, silty matrix		1.90	0.71	0.00	0.23	94.74	97.57
			WIPP Exhaust Shaft					
720.0	**051190-95**							
	Coating	A2	6.93	1.65	5.81	4.67	69.43	88.49
	Matrix		4.80	0.81	0.00	0.67	92.11	98.39
721.0	**ESM-147**							
	Coating	A12	(11.33)	10.57	5.18	6.95	56.94	90.97
	Matrix		6.20	1.01	1.53	1.01	93.10	102.84
ESM161372-woclt250u								
Black shale beneath Culebra			76.00	10.94	6.30	0.98	-0.18	94.04
			Drill hole H19b7					
742.85	**H19b7-742.85**							
	Coating	C1	22.67	2.97	13.78	2.04	53.31	94.78
	Matrix		26.93	1.84	12.84	0.52	56.29	98.43
744.6	**H19b7-744.6**							
	Coating	D1	16.53	4.14	1.71	0.93	74.48	97.80
	Matrix		12.40	3.05	1.60	0.66	80.19	97.90
	Coating, EDTA res.		73.60	32.13	0.00	0.25	0.75	106.74
752.0	**H19b7-752.0**							
	Coating	A21	5.00	0.54	9.68	5.44	61.99	82.65
	Matrix		3.87	0.61	2.12	1.07	86.87	94.54
752.2	**H19b7-752.2**							
	Coating	A1	12.27	3.21	2.52	1.53	77.24	96.75
	Matrix		4.67	0.79	1.57	0.91	88.12	96.06

Table C-1. Continued.

Depth, ft	Sample ID	Type	Clay	Quartz	Gypsum	Dolomite	Halite	Total
			Drill hole H19b7					
754.7	**H19b7-754.7**							
	Coating	A12	4.40	0.14	1.03	1.34	91.40	98.30
	Matrix		2.13	0.56	0.26	0.63	94.79	98.36
755.0	**H19b7-755.0**							
	Coating	A1	5.07	-0.57	1.06	1.96	87.68	95.19
	Matrix		3.73	1.03	0.30	0.77	94.74	100.58
	Mtx., powdery		4.73	1.06	0.11	0.16	94.95	101.01
757.6	**H19b7-757.6**							
	Coating	D1	6.47	1.64	0.32	0.67	86.50	95.59
	Matrix		3.00	0.74	0.24	0.48	94.48	98.94
758.7	**H19b7-758.7**							
	Coating 1	A1	4.27	0.61	3.05	3.38	80.80	92.11
	Coating 2	D1	4.27	0.95	0.68	2.31	88.09	96.29
	Matrix		3.27	0.52	0.69	1.21	89.73	95.41
761.8	**H19b7-761.8**							
	Coating	A1	4.53	0.99	26.65	2.86	68.80	103.83
	Matrix		6.53	-1.07	37.51	0.80	55.83	99.60

Intentionally Left Blank

Appendix D. Analytical Electron Microprobe Analyses of fine-grained clay mixtures in the Culebra Dolomite

Polished thin sections of 14 samples of the Culebra dolomite from several different locations in and around the WIPP site were examined by analytical electron microprobe. Quantitative wavelength-dispersive microanalysis was carried out with a JEOL 733 Superprobe on fine-grained clay mixtures occurring in fracture coatings the dolomite matrix of the samples. Results of the AEM analyses are given below. Also given are analyses of detrital micas. Analytical variability was determined from counting statistics. Errors are ±2% for elements present in concentrations greater than 1%, and ±10% for elements present in concentrations of 1.0–0.1%. Reported values below 0.1% are order-of-magnitude estimates. Values below the detection limit are labeled "bd." Low totals are due to decrepitation and water loss during analysis (a common problem when analyzing poorly-crystalline hydrous phases) and because carbon (present as organic material in many samples) was not included in the analysis. Samples from fracture coatings are designated "fracture"; those from the dolomite matrix are "matrix."

Table D-1. AEM analyses of fine-grained clay mixtures in the Culebra.

Depth, ft	Sample #	SiO_2	Al_2O_3	TiO_2	MgO	Fe_2O_3*	MnO	CaO	Na_2O	K_2O	P2O5	SO3	Cl	Total
						Drill hole H2b								
637.0	**051190-109**													
	clay3 (fracture)	30.86	9.48	0.11	18.07	1.75	bd	0.54	0.12	1.55	bd	0.63	0.50	63.62
	clay4 (fracture)	24.05	6.47	bd	19.69	1.09	bd	0.82	0.42	0.49	bd	0.59	1.69	55.30
	clay6 (fracture)	28.89	8.19	0.17	19.21	1.21	bd	0.62	0.06	0.89	bd	0.71	0.35	60.31
	clay7 (fracture)	36.37	12.42	0.31	21.90	1.86	bd	0.41	0.21	1.71	0.69	0.59	0.31	76.77
	clay8 (fracture)	33.14	12.06	0.23	18.22	1.90	0.02	1.12	0.21	2.10	0.49	0.58	0.68	70.74
	clay10 (fracture)	34.43	11.02	0.10	22.07	1.78	0.04	0.77	0.17	1.35	0.12	0.70	0.17	72.71
						Drill hole H12								
843.5	**051190-98**													
	clay1 (matrix)	38.02	15.42	0.79	12.88	3.50	bd	0.31	0.22	4.14	0.08	0.62	0.29	76.27
	clay2 (matrix)	31.81	10.98	0.19	13.00	3.01	bd	0.30	0.13	2.73	0.05	0.55	0.29	63.05
						Drill hole H14								
554.0	**051190-62**													
	clay1 (matrix)	27.39	9.13	0.14	12.69	2.01	bd	0.81	0.15	2.06	bd	0.32	0.48	55.08
	clay2 (matrix)	30.84	9.89	0.74	10.75	3.98	0.04	0.26	0.28	3.47	0.29	0.11	0.34	61.00
	clay4 (matrix)	24.90	7.94	0.05	13.73	1.33	bd	0.47	0.15	1.23	0.12	0.31	0.47	50.70
	clay5 (matrix)	28.12	9.09	0.07	15.97	1.66	bd	0.55	0.26	1.46	0.28	0.19	0.18	57.84

Table D-1. Continued..

Depth, ft	Sample #	SiO_2	Al_2O_3	TiO_2	MgO	Fe_2O_3*	MnO	CaO	Na_2O	K_2O	P2O5	SO3	Cl	Total
						Drill hole H15								
879.8	**051090-26**													
	clay1 (fracture)	34.33	11.54	0.42	20.58	1.70	bd	0.55	0.14	1.57	bd	0.93	0.13	71.88
	clay2 (fracture)	26.19	8.59	0.03	12.67	1.59	bd	0.46	bd	1.33	bd	0.47	0.47	51.86
	clay3 (fracture)	35.77	12.45	0.06	13.23	4.72	0.04	0.85	0.14	4.23	bd	1.48	0.46	73.43
						Drill hole H16								
705.0	**051190-80**													
	clay1 (matrix)	43.70	16.00	0.19	16.19	3.04	0.02	0.27	0.78	3.82	0.11	0.38	0.13	84.62
	clay2 (matrix)	38.47	13.11	0.24	13.25	3.10	0.04	1.06	0.49	3.97	bd	0.22	0.18	74.13
	clay3 (matrix)	40.46	14.48	0.24	18.20	3.17	bd	0.08	0.67	3.06	bd	0.20	0.13	80.70
	clay4 (matrix)	35.59	11.22	0.32	19.16	2.87	bd	0.14	0.52	2.20	bd	0.23	0.22	72.47
	clay5 (matrix)	38.47	11.77	0.50	13.67	3.68	bd	0.14	0.37	3.34	bd	0.17	0.23	72.32
						Drill hole H18								
692.9	**051090-44**													
	clay1 (matrix)	35.24	10.33	2.31	19.59	2.43	bd	0.63	0.08	1.20	0.06	0.30	0.14	72.32
	clay2 (fracture)	28.88	9.00	0.16	14.37	11.12	bd	0.30	0.22	1.62	bd	0.36	0.18	66.22
	clay3 (fracture)	30.83	9.61	0.49	19.37	8.52	bd	0.51	0.39	1.59	1.14	0.42	0.05	72.93
	clay4 (fracture)	29.08	10.66	0.29	9.45	17.66	0.10	0.57	0.53	2.69	1.19	0.32	0.42	72.96
	clay6 (matrix)	37.28	10.84	0.07	21.97	1.79	bd	0.37	0.70	1.26	0.62	0.34	0.17	75.41
	clay8 (matrix)	34.68	11.62	0.10	15.59	2.39	bd	0.25	0.88	2.36	0.48	0.33	0.30	68.98
696.9	**051090-46**													
	clay3 (matrix)	37.32	15.48	0.28	11.04	3.14	0.04	0.34	0.35	4.60	0.16	bd	0.17	72.91
	clay4 (matrix)	32.34	12.75	0.29	13.26	2.93	0.03	0.37	0.29	2.59	bd	0.64	0.12	65.62
	clay5(matrix)	32.85	14.28	0.58	10.09	4.48	0.05	0.37	0.36	3.13	bd	bd	0.15	66.34
694.2	**051090-47**													
	clay1 (fracture)	40.85	16.29	0.36	16.25	3.24	0.05	0.27	0.42	3.63	0.04	0.12	0.13	81.64
	clay2 (fracture)	36.77	12.48	0.23	17.62	2.61	0.07	0.97	0.33	2.28	0.24	0.29	0.09	73.97
	clay3 (fracture)	33.45	10.65	0.24	16.71	2.77	0.02	0.27	0.21	1.75	0.03	0.17	0.14	66.41
	Muscovite1	46.41	28.27	0.74	2.22	6.39	0.09	0.36	0.15	7.40	0.02	bd	bd	92.05
	Biotite1	31.82	15.96	1.25	10.05	16.10	0.03	0.36	0.26	6.36	0.06	0.31	0.31	82.74
	Biotite2	31.73	16.68	1.29	9.81	17.32	0.05	0.21	0.21	6.76	0.07	bd	bd	84.20
695.7	**051090-48**													
	clay1 (fracture)	27.88	12.42	0.39	9.24	34.80	0.16	0.39	0.26	2.74	0.18	0.27	0.11	88.84
	clay2 (fracture)	37.57	13.81	0.23	18.30	8.10	0.06	0.39	0.26	2.43	0.05	0.13	0.26	81.59
	clay3 (matrix)	38.55	13.38	0.19	20.10	2.88	bd	0.46	0.26	2.10	0.03	0.26	0.14	78.34
	clay4 (matrix)	40.26	15.52	0.32	15.35	3.64	bd	0.82	0.27	3.73	0.04	0.23	0.13	80.30

Table D-1. Continued..

Depth, ft	Sample #	SiO_2	Al_2O_3	TiO_2	MgO	Fe_2O_3*	MnO	CaO	Na_2O	K_2O	P2O5	SO3	Cl	Total
						Drill hole WIPP-19								
770.1	**051190-119**													
	clay3 (fracture)	39.06	10.36	0.06	13.41	8.08	0.03	0.84	0.19	4.20	0.14	0.55	0.54	77.46
	clay4 (fracture)	37.06	14.47	1.33	17.01	3.36	0.02	0.28	0.43	3.17	0.03	1.22	0.50	78.89
	clay5 (fracture)	32.18	13.31	0.45	10.05	3.08	0.03	1.32	0.23	3.72	bd	0.36	0.35	65.06
						WIPP Exhaust Shaft								
721.0	**ESM-147**													
	clay1 (fracture)	31.39	10.31	2.26	17.07	2.62	bd	0.24	0.33	1.87	bd	0.15	0.18	66.44
	clay2 (matrix)	32.99	10.97	0.35	15.23	2.40	bd	0.27	0.15	2.26	bd	0.22	0.14	64.97
	clay3 (matrix)	30.54	9.54	0.17	16.56	1.95	bd	0.32	0.07	1.46	bd	0.34	0.25	61.21
						Drill hole H19b7								
744.6	**H19b7-744.6**													
	clay1 (matrix)	35.86	12.60	0.96	15.01	3.22	0.05	0.99	0.26	3.29	0.18	0.25	0.13	72.77
	clay2 (matrix)	38.69	11.92	0.07	20.39	2.10	bd	0.34	0.29	2.19	0.22	0.44	0.17	76.83
	clay3 (matrix)	37.98	12.19	0.60	19.45	2.11	bd	0.16	0.21	2.18	bd	0.41	0.19	75.48
	clay4 (matrix)	26.26	6.94	bd	20.47	0.85	bd	1.00	0.23	0.20	bd	0.28	0.13	56.37
	clay5 (matrix)	31.72	10.25	0.48	10.97	2.97	bd	0.36	0.33	3.34	bd	0.30	0.28	60.99
752.2	**H19b7-752.2**													
	clay1 (fracture)	37.82	14.45	0.27	16.07	3.38	0.03	0.36	0.17	3.20	0.25	0.45	0.19	76.64
	clay2 (fracture)	37.03	12.45	0.87	23.89	1.63	bd	0.31	0.09	1.34	0.12	0.62	0.22	78.55
	clay3 (fracture)	37.97	13.25	0.16	22.90	2.23	bd	0.25	0.14	1.83	0.23	0.63	0.14	79.72
	clay4 (matrix)	33.68	12.08	0.68	16.25	2.89	0.03	1.09	0.13	2.63	0.05	1.13	0.31	70.95
	clay5 (matrix)	31.92	10.41	0.13	20.21	1.74	bd	1.33	0.34	1.54	0.30	0.70	0.37	69.00
757.6	**H19b7-757.6**													
	clay2 (matrix)	29.96	10.44	0.09	16.50	1.44	bd	1.12	0.18	1.94	0.10	0.66	0.22	62.65
	clay3 (matrix)	30.96	10.38	0.11	18.49	1.03	bd	0.38	0.11	1.48	bd	0.62	0.21	63.76
	clay5 (matrix)	31.40	9.63	0.25	18.58	1.81	bd	0.41	0.17	2.14	0.31	0.94	0.26	65.91
	clay6 (matrix)	29.67	7.42	0.07	19.68	1.00	bd	0.39	0.09	0.88	bd	0.88	0.28	60.36
	clay7 (matrix)	32.52	11.16	0.08	18.60	2.04	bd	0.25	0.20	1.93	bd	0.73	0.36	67.88
	clay8 (matrix)	34.23	13.51	0.21	8.66	3.43	bd	0.28	0.22	4.55	0.09	0.21	0.24	65.64

Intentionally Left Blank

Appendix E. Calculated Clay Concentrations Per Unit Area On Surfaces Within the Culebra

As matrix material was incorporated into the coating samples during sample collection, the amount of clay in the coating samples is not a direct measure of the amount of clay on the fracture surface. However, this value may be estimated from the modal mineral contents of the coating sample and the adjacent matrix sample in the following manner:

$clay_{cs}$ — mass of clay in a coating sample
$dolo_{cs}$ — mass of dolomite in the coating sample
m_{cs} — mass of the coating sample
$f_{cs\text{-}c}$ — modal clay content of the coating sample
$f_{cs\text{-}d}$ — modal dolomite content in the coating sample
$clay_{coat}$ — mass of clay in the fracture coating material
m_{coat} — mass of fracture coating material *in the coating sample*
f_{coat} — modal clay content of the fracture coating
$clay_{mtx}$ — mass of clay in the matrix material *in the coating sample*
$dolo_{mtx}$ — mass of dolomite in the matrix material *in the coating sample*
m_{mtx} — mass of matrix material *in the coating sample*
$f_{mtx\text{-}c}$ — modal clay content of the matrix material
$f_{mtx\text{-}d}$ — modal dolomite content in the matrix

The clay in a particular coating sample is the mass of the sample multiplied by the weight fraction of the sample that is clay:

$$clay_{cs} = m_{cs} \times f_{cs\text{-}c} \qquad \text{eq. (1)}$$

It is also equal to the amount of clay in the actual fracture coating plus the amount in the matrix material that was incorporated into the coating sample (see Figure 2):

$$clay_{cs} = clay_{coat} + clay_{mtx} \qquad \text{eq. (2)}$$

Rearranging, and formulating $clay_{mtx}$ as in eq. (1) above gives:

$$clay_{coat} = (m_{cs} \times f_{cs\text{-}c}) - (m_{mtx} \times f_{mtx\text{-}c}) \qquad \text{eq. (3)}$$

Of these variables, m_{cs} and $f_{cs\text{-}c}$ are determined by analysis of the coating sample, and $f_{mtx\text{-}c}$ is assumed to be that measured from the accompanying matrix sample. The mass of matrix material in the coating sample, m_{mtx}, can be estimated from the modal dolomite composition of the coating sample. If we assume that all of the dolomite was contributed by the incorporated matrix:

$$dolo_{cs} = dolo_{mtx} \qquad \text{eq. (4)}$$

or,

$$m_{cs} \times f_{cs\text{-}d} = m_{mtx} \times f_{mtx\text{-}d} \quad \text{eq. (5)}$$

Solving for m_{mtx} and substituting this into eq. (3) yields:

$$clay_{coat} = (m_{cs} \times f_{cs\text{-}c}) - [(m_{cs} \times f_{cs\text{-}d})/f_{mtx\text{-}d}] \times f_{mtx\text{-}c} \quad \text{eq. (6)}$$

Assuming that all the modal dolomite in the coating sample came from the incorporated matrix material results in a *minimum* estimate of the amount of clay on the fracture surface.

The estimated amount of clay on the fracture was then divided by the surface area from which the sample was taken to yield the amount of clay per unit area:

$$\text{Clay per unit area, g/m}^2 = [(\text{Clay, g})/(\text{Sampled area, cm}^2)] * (10{,}000\ \text{cm}^2/\text{m}^2) \quad \text{eq. (7)}$$

Table E-1. Calculated Clay Concentrations on Surfaces Within the Culebra

Depth, ft	Sample ID	Surface Type	Surface Area, cm^2	Clay on surface, g	Clay on surface, g/m^2
Borehole H2b					
632.0	051190-107	C12	12.37	0.025	20.3
637.0	051190-109	B21	14.14	0.011	7.8
Borehole H14					
547.9	051190-59	C1	22.97	0.094	41.0
553.4	051190-61	D1	22.97	2.23	971
554.0	051190-62-S1	A21	20.00	0.002	1.1
554.0	051190-62-S2	A12	44.00	0.008	1.8
Borehole H15					
870.5	051090-22	B1	27.27	0.123	44.9
879.8	051090-26	B1	47.12	0.004	0.9
877.7	051090-28	B1	70.69	0.145	20.9
Borehole H16					
705.0	051190-80-S1	A12	21.21	0.030	14.3
705.0	051190-80-S2	D1	23.00	11.6	5070
708.0	051190-82	B1	21.21	0.009	4.3
704.8	051190-83	C1	22.97	0.284	123
718.1	051190-86	C1	10.60	0.001	0.7
713.2	051190-84	B1	22.97	0.037	16.0
Borehole H18					
692.9	051090-44	A12	28.27	0.295	104
696.9	051090-46	A2	24.74	0.001	0.5
694.2	051090-47	A21	36.00	0.058	16.1
695.7	051090-48	A1	48.14	0.177	36.7
Borehole WIPP-19					
770.1	051190-119	C1	8.75	0.007	8.2

Table E-1. Continued.

Depth, ft	Sample ID	Surface Type	Surface Area, cm^2	Clay on surface, g	Clay on surface, g/m^2
Exhaust Shaft					
720.0	051190-95	A2	126.00	0.024	1.9
721.0	ESM-147	A12	56.00	0.020	3.6
Borehole H19b7					
742.85	H19b7-742.85	C1	26.00	-0.062	-23.8
744.6	H19b7-744.6	D1	40.21	0.835	207.6
752.0	H19b7-752.0	A21	45.00	0.008	1.8
752.2	H19b7-752.2	A1	59.00	0.158	26.7
754.7	H19b7-754.7	A12	33.00	0.012	3.6
755.0	H19b7-755.0	A1	61.00	0.004	0.7
757.6	H19b7-757.6	D1	13.00	0.324	250
758.7	H19b7-758.7-1	A1	40.00	0.005	1.3
758.7	H19b7-758.7-2	D1	44.00	0.029	6.6
761.8	H19b7-761.8	A1	37.00	-0.011	-3.0